



**HAL**  
open science

## Period spacings in red giants

B. Mosser, C. Gehan, K. Belkacem, R. Samadi, E. Michel, M.-J. Goupil

► **To cite this version:**

B. Mosser, C. Gehan, K. Belkacem, R. Samadi, E. Michel, et al.. Period spacings in red giants. *Astronomy & Astrophysics - A&A*, 2018, 618, pp.A109. 10.1051/0004-6361/201832777 . hal-01321683

**HAL Id: hal-01321683**

**<https://hal.sorbonne-universite.fr/hal-01321683v1>**

Submitted on 17 Dec 2018

**HAL** is a multi-disciplinary open access archive for the deposit and dissemination of scientific research documents, whether they are published or not. The documents may come from teaching and research institutions in France or abroad, or from public or private research centers.

L'archive ouverte pluridisciplinaire **HAL**, est destinée au dépôt et à la diffusion de documents scientifiques de niveau recherche, publiés ou non, émanant des établissements d'enseignement et de recherche français ou étrangers, des laboratoires publics ou privés.

# Period spacings in red giants<sup>★</sup>

## IV. Toward a complete description of the mixed-mode pattern

B. Mosser<sup>1</sup>, C. Gehan<sup>1</sup>, K. Belkacem<sup>1</sup>, R. Samadi<sup>1</sup>, E. Michel<sup>1</sup>, M-J. Goupil<sup>1</sup>

LESIA, Observatoire de Paris, PSL Research University, CNRS, Université Pierre et Marie Curie, Université Paris Diderot, 92195 Meudon, France; benoit.mosser@obspm.fr

### ABSTRACT

*Context.* Oscillation modes with a mixed character, as observed in evolved low-mass stars, are highly sensitive to the physical properties of the innermost regions. Measuring their properties is therefore extremely important to probe the core, but requires some care, due to the complexity of the mixed-mode pattern.

*Aims.* The aim of this work is to provide a consistent description of the mixed-mode pattern of low-mass stars, based on the asymptotic expansion. We also study the variation of the gravity offset  $\varepsilon_g$  with stellar evolution.

*Methods.* We revisit previous works about mixed modes in red giants and empirically test how period spacings, rotational splittings, mixed-mode widths, and heights can be estimated in a consistent view, based on the properties of the mode inertia ratios.

*Results.* From the asymptotic fit of the mixed-mode pattern of a large set of red giants at various evolutionary stages, we derive unbiased and precise asymptotic parameters. As the asymptotic expansion of gravity modes is verified with a precision close to the frequency resolution for stars on the red giant branch ( $10^{-4}$  in relative values), we can derive accurate values of the asymptotic parameters. We decipher the complex pattern in a rapidly rotating star, and explain how asymmetrical splittings can be inferred. We also revisit the stellar inclinations in two open clusters, NGC 6819 and NGC 6791: our results show that the stellar inclinations in these clusters do not have privileged orientation in the sky. The variation of the asymptotic gravity offset with stellar evolution is investigated in detail. We also derive generic properties that explain under which conditions mixed modes can be observed.

**Key words.** Stars: oscillations - Stars: interiors - Stars: evolution

### 1. Introduction

Probing the cores of stars is difficult since, generally, stellar information arises from their photosphere. Fortunately, asteroseismology of evolved stars reveals stellar interiors in a unique and powerful way: gravity waves that propagate throughout the core couple with pressure waves and construct mixed modes that can be observed (Beck et al. 2011; Bedding et al. 2011; Benomar et al. 2014). The measurement of the global seismic properties of these mixed modes then carries unique information on the core structure (e.g., Montalbán et al. 2013; Lagarde et al. 2016; Bossini et al. 2015, 2017). Observations with the space missions CoRoT and *Kepler* have provided the measurement of the asymptotic period spacings (Mosser et al. 2012b; Vrad et al. 2016), of the differential-rotation profile in red giants (Beck et al. 2012; Deheuvels et al. 2014, 2015), and of the core rotation for about 300 stars analyzed by Mosser et al. (2012c).

Most of the previous studies are based on the measurement and analysis of global seismic parameters, such as the asymptotic large separation  $\Delta\nu$  and the asymptotic period spacings  $\Delta\Pi_1$  (e.g., Miglio et al. 2017). It is now time to access the properties of individual frequencies in red giants. Up to now, most of the studies (e.g., Baudin et al. 2012; Di Mauro et al. 2016) were limited to stars on the red giant branch (RGB). Two main reasons explain this restriction: first, the oscillation spectra benefit from a better relative frequency resolution for this evolutionary stage; second, the

oscillation spectra remain simple, with rotational splittings smaller than period spacings. When stars evolve, these features become intricate, so that confusion is possible. For the most evolved stars, mixed modes are no longer observable (e.g., Baudin et al. 2012; Mosser et al. 2013; Stello et al. 2014).

The understanding of any complicated mixed-mode oscillation pattern must be based on an unambiguous identification of the modes. Up to now, the most efficient method has relied on the use of the asymptotic expansion, completed by a clear description of the influence of rotation (Mosser et al. 2015). New insights on rotation were provided by the analysis depicted in Gehan et al. (2016), who have developed a methodology to measure rotational splittings in an automated way; Gehan et al. (2017) and Gehan et al. (2018) showed how rapid rotation can be addressed efficiently. This efficiency derives from the use of stretched oscillation spectra.

In this work, we first examine in Section 2 how the different frequency spacings in the asymptotic mixed-mode expansion can be expressed as a function of the mode inertia. New expressions are proposed for the mixed-mode spacings and rotational splittings. Case studies are examined in Section 3 to test and validate these expressions. In Section 4, we take advantage of the precision of the fits to derive accurate asymptotic period spacings and gravity offsets; for the first time, we can exhibit the global evolution of

these gravity offsets as a function of stellar evolution. New insights on the rotational splittings are proposed in Section 5; in particular, we show how the asymptotic expansion can be used to provide priors based upon physical assumptions for any fitting code used later in the analysis. Finally, we assess the conditions for observing mixed modes, based on global asymptotic parameters only (Section 6). Section 7 is devoted to our conclusions.

## 2. Mixed-mode parameters

Following the work of Shibahashi (1979) and Unno et al. (1989), we derived asymptotic expansions of mixed modes for different seismic parameters: eigenfrequencies (Mosser et al. 2012b), period spacings (Christensen-Dalsgaard 2012), rotational splittings (Goupil et al. 2013; Deheuvels et al. 2015), and mode widths and mode heights (Grosjean et al. 2014; Belkacem et al. 2015b,a; Mosser et al. 2017a). Here, we intend to revisit all these parameters that depict the mixed-mode spectrum in order to provide a more precise and unified view.

### 2.1. Asymptotic expansion

The asymptotic expansion of mixed modes is an implicit relation between the phases  $\theta_p$  and  $\theta_g$  of the pressure- and gravity-wave contributions to the mixed modes, respectively. It reads

$$\tan \theta_p = q \tan \theta_g, \quad (1)$$

where  $q$  is the coupling factor (Mosser et al. 2017b). The phases are related to the large separation  $\Delta\nu$  and the period spacing  $\Delta\Pi_1$ . The most convenient expressions of the phase refer respectively to the pure<sup>1</sup> p and g mode spectra

$$\theta_g = \pi \frac{1}{\Delta\Pi_1} \left( \frac{1}{\nu} - \frac{1}{\nu_g} \right), \quad (2)$$

$$\theta_p = \pi \frac{\nu - \nu_p}{\Delta\nu_p}, \quad (3)$$

where  $\nu_p$  and  $\nu_g$  are the asymptotic frequencies of pure pressure and gravity modes, respectively, and  $\Delta\nu_p$  is the frequency difference between the consecutive pure pressure radial modes with radial orders  $n_p$  and  $n_p + 1$ . In this work, we consider that the radial modes and pure dipole pressure modes obey the universal red giant oscillation pattern (Mosser et al. 2011b) and that the dipole gravity modes follow the asymptotic comb-like pattern

$$\frac{1}{\nu_g} = (-n_g + \varepsilon_g) \Delta\Pi_1, \quad (4)$$

where  $\Delta\Pi_1$  is the period spacing and  $\varepsilon_g$  is the gravity offset.

Mosser et al. (2015) derived that the variation of the oscillation period  $P$  with the mixed radial order  $n$  writes

$$\frac{dP}{dn} = \zeta \Delta\Pi_1. \quad (5)$$

<sup>1</sup> Pure p (or g) modes are hypothetical modes that could be formed in the pressure (or gravity) cavity without any coupling with the other cavity.

A convenient way to write the parameter  $\zeta$  is (Hekker & Christensen-Dalsgaard 2017)

$$\zeta(\nu) = \left[ 1 + \frac{q}{\mathcal{N}} \frac{1}{q^2 \cos^2 \theta_p + \sin^2 \theta_p} \right]^{-1}, \quad (6)$$

where  $\mathcal{N} = \Delta\nu/(\nu^2 \Delta\Pi_1)$  is the density of gravity modes compared to pressure modes, in other words the number of mixed modes in a  $\Delta\nu$ -wide interval. Compared to the original form presented in Mosser et al. (2015), the rapidly varying phase  $\theta_g$  has been replaced by a function of  $\theta_p$  that varies in a smooth way.

As demonstrated by Goupil et al. (2013) and used by subsequent work (Benomar et al. 2014; Deheuvels et al. 2015), the function  $\zeta$  is connected to the inertia of mixed modes. Introducing the contributions of the envelope and of the core,

$$\zeta = \frac{I_{\text{core}}}{I_{\text{env}} + I_{\text{core}}}, \quad (7)$$

and assuming that the envelope contribution of a mixed mode is similar to the inertia of the closest radial mode ( $I_{\text{env}} \equiv I_{n_p,0}$ ), we find that the inertia of the dipole mode with mixed radial order  $n$  varies as

$$I_{n,1} = \frac{I_{n_p,0}}{1 - \zeta}. \quad (8)$$

For the sake of simplicity, we use hereafter the abridged notation  $I_n$  for the inertia of the dipole mixed modes and  $I_0$  for the closest radial modes, and follow the same convention for the mode heights and widths.

### 2.2. Seismic parameters

With  $\zeta$ , we now intend to express the different seismic parameters.

#### 2.2.1. Period spacing

Following Christensen-Dalsgaard (2012) and Mosser et al. (2015), period spacings can be expressed as

$$\Delta P = P_n - P_{n+1} = \zeta \Delta\Pi_1. \quad (9)$$

This expression is however ambiguous, since  $\zeta$  may vary significantly between the periods  $P_{n+1}$  and  $P_n$  ( $> P_{n+1}$ ). Therefore, we prefer to consider the expression resulting from the integration of Eq. (5)

$$\Delta P = P_n - P_{n+1} = \Delta\Pi_1 \int_n^{n+1} \zeta(\nu) dn = \Delta\Pi_1 \langle \zeta \rangle_n, \quad (10)$$

where we consider that the mixed-mode radial order  $n$  is a continuous variable defined by  $dn = d\tau/\Delta\Pi_1$ , where  $\tau$  is the stretched period introduced by Mosser et al. (2015); i.e.,

$$d\tau = \frac{d\nu}{\zeta \nu^2}. \quad (11)$$

In fact,  $n$  takes consecutive integer values for each mixed mode. In this work, we use an estimate of  $n = n_p + n_g$  derived from the pressure and gravity radial orders;  $n_p$

is derived from the universal red giant oscillation pattern (Mosser et al. 2011b), whereas  $n_g$  is given by

$$n_g = - \left[ \frac{1}{\nu \Delta \Pi_1} - \frac{1}{4} \right] \quad \text{on the RGB,} \quad (12)$$

$$n_g = - \left[ \frac{1}{\nu \Delta \Pi_1} + \frac{1}{4} \right] \quad \text{in the red clump,} \quad (13)$$

where the correcting terms  $\pm 1/4$  that depend on the evolutionary stage are justified in Section 4.4. They differ by  $1/2$ , as depicted by the asymptotic relation (e.g., Tassoul 1980; Benomar et al. 2013). In red giants, the high density  $\mathcal{N}$  of mixed modes implies that  $|n_g| \gg n_p$ , so that the mixed-mode orders are negative.

From the definition of the stretched period, Eq. (10) reduces to

$$\Delta P = \int_{\nu_n}^{\nu_{n+1}} \frac{d\nu}{\nu^2}. \quad (14)$$

This evident relation justifies the relevance of Eq. (10) instead of Eq. (9): using  $\langle \zeta \rangle_n$  is necessarily more accurate than using  $\zeta$  for computing period spacings.

### 2.2.2. Rotational splitting

As introduced by Goupil et al. (2013), the function  $\zeta$  is used to express the mixed-mode rotational splitting as a function of the mean rotational splittings related to pure gravity or pure pressure modes:

$$\delta \nu_{\text{rot}} = \zeta \delta \nu_{\text{rot,g}} + (1 - \zeta) \delta \nu_{\text{rot,p}}. \quad (15)$$

As shown by subsequent works (e.g., Deheuvels et al. 2014; Di Mauro et al. 2016; Triana et al. 2017), it is difficult to derive from the observed rotational splittings more than these two mean quantities.

Again, we have to solve the ambiguity of the meaning of  $\zeta$  in Eq. (15), since we can either consider the value<sup>2</sup>  $\zeta(\nu_{n,0})$ , in the framework of the perturbation of the non-rotating frequency  $\nu_{n,0}$ , or  $\zeta(\nu_{n,m})$ , considering that the inertia to be considered corresponds to the actual frequency  $\nu_{n,m}$ . By analogy with the equation dealing with the period spacing, we propose to rewrite the rotational splitting  $\delta \nu_{\text{rot}} = \nu_{n,m} - \nu_{n,0}$ , in the limit case where the mean envelope rotation is negligible compared to the mean core rotation, as

$$\delta \nu_{\text{rot}} = \delta \nu_{\text{rot,core}} \int_{\nu_{n,0}}^{\nu_{n,m}} \zeta \, dm = \delta \nu_{\text{rot,core}} \langle \zeta \rangle_m, \quad (16)$$

where  $\delta \nu_{\text{rot,core}} \equiv \delta \nu_{\text{rot,g}}$ . As for the radial order  $n$  in Eq. (10), we consider the azimuthal order  $m$  as a continuous variable varying from 0 to  $\pm 1$ . So, we have introduced two mean values of  $\zeta$ ,

$$\langle \zeta \rangle_n = \int_n^{n+1} \zeta \, dn = \int_{\nu_{n,m}}^{\nu_{n+1,m}} \frac{d\nu}{\Delta \Pi_1 \nu^2}, \quad (17)$$

$$\langle \zeta \rangle_m = \int_0^{\pm 1} \zeta \, dm = \int_{\nu_{n,0}}^{\nu_{n,\pm 1}} \frac{d\nu}{\Delta \Pi_1 \nu^2}, \quad (18)$$

to account for the period spacings and rotational splittings. The relevance of  $\langle \zeta \rangle_n$  is already proven by Eqs. (10) and

<sup>2</sup> Since we consider dipole modes only, we use a simplified notation  $\nu_{n,m}$  instead of  $\nu_{n,\ell,m}$ .

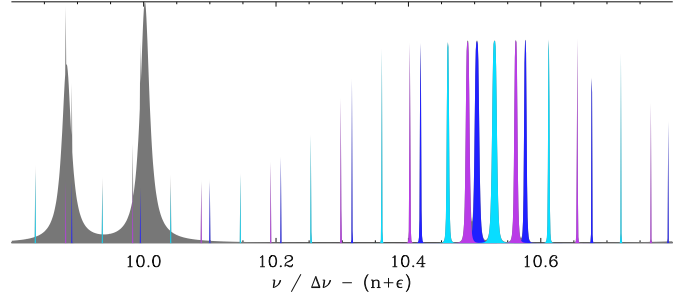


**Fig. 1.** Description of the radial order closest to  $\nu_{\text{max}}$  of the oscillation power spectrum of a typical RGB star. Frequencies, widths, and heights are estimated according to the function  $\zeta$ . Quadrupole and radial modes are plotted in gray, dipole mixed modes in dark blue ( $m = -1$ ), light blue ( $m = 0$ ), or purple ( $m = 1$ ), respectively.

(11), whereas the relevance of  $\langle \zeta \rangle_m$  has yet to be demonstrated. If we succeed, we will also have understood the relevance of the use of stretched periods for analyzing the mixed modes (Eq. 11).

### 2.3. Mixed-mode width, height, and amplitude

The work performed by the gas during one oscillation cycle is the same for all modes, associated with surface damping, when the radiative damping in the Brunt-Väisälä cavity is considered as negligible. Hence, Benomar et al. (2014) have estimated that the mode width of the mixed modes writes

$$\Gamma_n = \Gamma_0 \frac{I_0}{I_n} = \Gamma_0 (1 - \zeta). \quad (19)$$

From this relation, we verify that mixed modes have smaller mode widths than radial modes. However, we recall that a family of stars behave differently, when mixed modes are depressed because of an extra damping in the radiative inner region (Mosser et al. 2012a; García et al. 2014; Mosser et al. 2017a).

From Belkacem et al. (2015a) we also derive that the amplitude of a resolved dipole mixed mode is

$$A_n^2 = A_0^2 (1 - \zeta), \quad (20)$$

when the geometrical factor that conducts to a visibility of about 1.54 for red giant dipole modes (Mosser et al. 2012a, 2017a) is omitted. Such amplitudes correspond to similar heights for radial and dipole modes since  $A^2 = \pi \Gamma H / 2$ . When, for non-resolved mixed modes, the width  $\Gamma_n$  is less than the frequency resolution  $\delta f_{\text{res}}$ , a dilution factor must be considered (Dupret et al. 2009). It expresses

$$H_n = \frac{\pi}{2} \frac{\Gamma_n}{\delta f_{\text{res}}} H_0, \quad (21)$$

when radial modes are resolved, which is the common case.

### 2.4. Synthetic mixed-mode pattern

The previous ingredients can be used to depict an oscillation pattern. Figure 1 shows the synthetic spectrum of a typical star on the low RGB, based on Eq. (16) for the rotational splittings, on Eq. (19) for the mode widths, and on Eq. (21) for the mode heights of unresolved modes. This spectrum resembles the description derived by Grosjean

et al. (2014) from non-adiabatic computations, with a time-dependent treatment of convection which provides the lifetimes of radial and non-radial mixed modes.

### 3. Case studies

In this Section, we use RGB stars showing clear oscillation spectra as case studies, in order to test the description of the mixed-mode spacings, widths, heights, and rotational splittings, which were previously introduced. The first steps consist in identifying their oscillation spectra and in fitting as many dipole mixed modes as possible. One of the two stars considered here, KIC 6144777 was already investigated in many previous articles (e.g., Corsaro et al. 2015; García Saravia Ortiz de Montellano et al. 2018). The other one, KIC 3955033, was less studied since it shows a complicated mixed-mode spectrum; it belongs to the list of red giants with period spacings automatically computed by Vrad et al. (2016). We used data downloaded from the KASOC site<sup>3</sup>, processed using the *Kepler* pipeline developed by Jenkins et al. (2010), and corrected from outliers, occasional jumps, and drifts (see García et al. 2011, for details).

#### 3.1. Identification of the mixed modes

The location of the mixed modes primarily relies on the firm identification of the pure pressure-mode spectrum. The determination of the large separation  $\Delta\nu$ , first derived from the envelope autocorrelation function (Mosser & Appourchaux 2009), is based on the universal red giant oscillation pattern. This method provides the efficient identification of the radial modes and helps to locate the frequency ranges where mixed modes cannot be mistaken for radial or quadrupole modes. For  $\ell = 1$  modes, the second-order asymptotic expansion writes

$$\nu_p = \left( n_p + \varepsilon_p + \frac{1}{2} + d_{01} + \frac{\alpha}{2} [n_p - n_{\max}]^2 \right) \Delta\nu, \quad (22)$$

where  $\varepsilon_p$  is the acoustic offset,  $n_{\max} = \nu_{\max}/\Delta\nu - \varepsilon_p$ , and  $\alpha = 0.076/n_{\max}$ . The parameter  $d_{01}$  is function of the large separation, under the form  $A + B \log \Delta\nu$  (where  $\Delta\nu$  is expressed in  $\mu\text{Hz}$ ), with  $A = 0.0553$  and  $B = -0.036$ , as determined from the large-scale analysis along the RGB conducted by Mosser et al. (2014). The accurate determination of  $d_{01}$  is crucial for the determination of the pure dipole pressure modes, hence for the determination of the minima of the function  $\zeta$ . In that respect, the small modulation of the radial-mode pattern induced by the sound-speed glitches (Miglio et al. 2010; Vrad et al. 2015) must be considered also. Therefore, we fit the actual position of the radial modes first, then use them to refine the pure pressure dipole-mode frequencies according to

$$\nu_p = (\nu_{n_p,0} + \nu_{n_p+1,0})/2 + d_{01} (\nu_{n_p+1,0} - \nu_{n_p,0}). \quad (23)$$

The background parameters, derived as in Mosser et al. (2012a), are used to correct the granulation contribution in the frequency range around  $\nu_{\max}$ . Hence, mixed modes can be automatically identified in frequency ranges that have no radial and quadrupole modes when their heights

are significantly above the background. The automatic selection of the modes relies on a statistical test: the height-to-background ratio of the modes must be higher than a threshold level  $R_p$  in order to reject the null hypothesis to a low probability  $p$ . According to Appourchaux et al. (2006), the relation between  $R_p$  and  $p$  depends for long-lived modes on the observation duration  $T_{\text{obs}}$  and on the width  $\Delta\nu$  of the frequency range where a mode is expected. This relation expresses

$$R_p \simeq \ln \frac{T_{\text{obs}} \Delta\nu}{p}, \quad (24)$$

when expressed in noise unit. This situation applies here, since the precise identification of the mixed-mode pattern is based on gravity-dominated mixed modes. With 4-year observations and the search of a couple of modes in a frequency range  $\Delta\nu = \Delta\nu/\mathcal{N}$ , the threshold is typically 10 for a secure probability rejection at the  $10^{-2}$  level. In practice, mixed modes with a height-to-background ratio higher than 10 are used to initiate the fit. A lower threshold is enough for the final agreement, when the synthetic mixed-mode pattern based on secure modes can be used to search for long-lived mixed modes in narrow frequency ranges. We benefit from the fact that the asymptotic fit is precise and enables to search for thin modes in a frequency range  $\Delta\nu$  narrower than  $0.1 \mu\text{Hz}$ . Therefore, a threshold of 7 is enough for rejecting the null hypothesis at the 1%-level for these modes whose detection benefits from the information gained by larger peaks. The thin mode widths (Eq. 19) are of great use to map the observed spectrum: a thin gravity-dominated mixed mode must be found in the close vicinity, less than 4 times the mode width, of its expected position. For unresolved peaks, this condition is relaxed to 4 times the frequency resolution. The global seismic parameters of the gravity component are then derived from the methods described in Vrad et al. (2016) and Mosser et al. (2017b), with a least-square fit between the observed and asymptotic patterns.

At this stage, global seismic parameters are measured and mixed modes are identified, so that it is possible to measure their individual properties.

#### 3.2. Individual fitting procedure

When fitting individually mixed modes, we aim at testing the validity of the asymptotic expression, but not at reaching the ultimate precision, which is the role of a dedicated fit of individual modes (e.g., Gaulme et al. 2009). Therefore, in order to simplify the fit, we supposed (and checked a posteriori) that all multiplets can be fitted independently. This is not the case in all red giant spectra, but it is verified for most stars on the early RGB or in the red clump.

From the asymptotic fit, we identify in the background-corrected spectrum the power excess associated to each mode. Then, we determine the central frequency of the peak as the barycenter of the power excess. The height  $H$  and full width at half maximum  $\Gamma$  are simultaneously derived from the Lorentzian fit of the mode. We use Eqs. (19) and (21) as priors. Modes are fitted individually when the mode density is low, or simultaneously when the Lorentzians used as priors overlap.

The fitted spectrum and the seismic parameters of KIC 6144777, used as a first study case, are given in Fig. 2 and

<sup>3</sup> <http://kasoc.phys.au.dk>

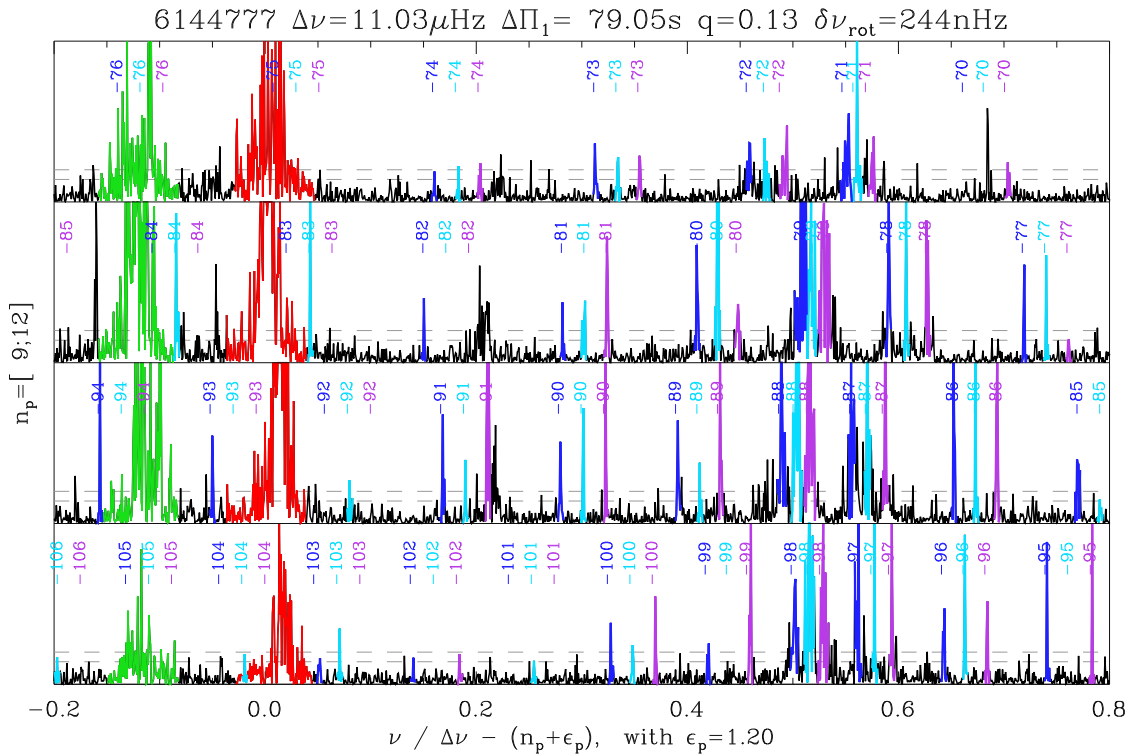


**Fig. 2.** Fit of the oscillation pattern of the RGB star KIC 6144777, showing the pressure radial orders  $n_p$  from 9 to 12. The power spectrum density has been divided by the fit of the background. Radial and quadrupole modes are highlighted in red and green. The expected locations of dipole mixed modes are labelled with their mixed radial orders. When detected, mixed modes are highlighted in dark blue ( $m = -1$ ), light blue ( $m = 0$ ), or purple ( $m = 1$ ).  $\ell = 3$  modes, which are also mixed, are located near the abscissa 0.22; extra peaks in the range  $[-0.2, -0.05]$  are mixed quadrupole modes. The gray dashed lines indicate the two thresholds used in this work, corresponding to height-to-background ratios of 7 and 10.

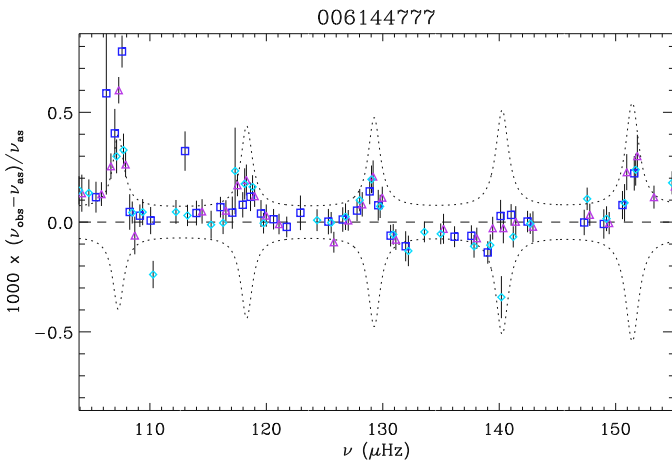


**Fig. 3.** Relative residuals, multiplied by 1000, between the observed and asymptotic mixed-mode frequencies in KIC 6144777. The color of the symbols indicates the azimuthal order: dark blue squares for  $m = -1$ , light blue diamonds for  $m = 0$ , or purple triangles for  $m = 1$ ;  $1\text{-}\sigma$  uncertainties are also shown. The dashed line corresponds to a perfect fit. The dotted lines show the frequency resolution plus an extra-modulation  $\Delta\nu(1 - \zeta)/100$ , which is empirically used to define the quality of the fit.

in Table A.1. We note the large agreement between the observed and asymptotic peaks. As in other stars showing a seismic signal with a high signal-to-noise ratio (S/R), outliers with a height-to-background value  $R$  higher than 7 are present. Their detection does not invalidate the method

presented above: they correspond either to  $\ell = 2$  or 3 mixed modes, possibly also to  $\ell = 4$  modes, or to aliases (since the duty cycle is about 93%), or even to noise since the detection of 1 noisy peak with  $R \geq 8$  is expected in a  $30\text{-}\mu\text{Hz}$  frequency range after 4 years of observation, assuming that the noise statistic is a  $\chi^2$  with two degrees of freedom.

The quality of the fit is shown by the small residuals between the observed frequencies and the asymptotic fits (Fig. 3); we note that these residuals are comparable to the uncertainties, derived from Libbrecht (1992) or slightly larger when the quality of the fit may be affected by the high mode density. These residuals are of about the frequency resolution. When pressure-dominated mixed modes are excluded, the standard deviation of the asymptotic fit is 11 nHz. This value represents 1.3 times the frequency resolution  $\delta f_{\text{res}}$ , or  $\Delta\nu/1000$ , or a relative precision at  $\nu_{\text{max}}$  of about  $10^{-4}$ . The quality of the fits is based on a small number of parameters: the radial mode frequencies, the mean location  $d_{01}$  of the expected pure pressure dipole modes, and four asymptotic parameters: the period spacing  $\Delta\Pi_1$ , the coupling factor  $q$ , gravitational offset  $\epsilon_g$ , and the mean core rotational splitting  $\delta\nu_{\text{rot}}$ . Residuals reach maximum values near the pressure-dominated mixed modes: there, deviations of about  $\Delta\nu/200$  are observed, to be compared to the amplitudes of pressure glitches of about  $\Delta\nu/40$  (Vrard et al. 2015). We suspect that these residuals are mostly due to the variation of the parameter  $d_{01}$  with frequency.

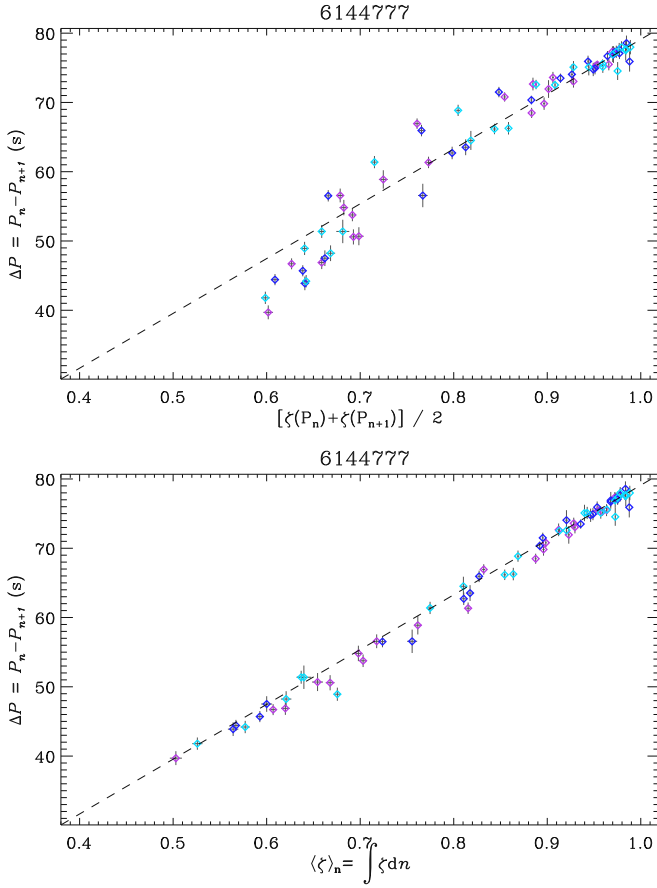


**Fig. 4.** Period spacings of the RGB star KIC 6144777. *Top*: plot as a function of the arithmetical mean value  $(\zeta(\nu_n) + \zeta(\nu_{n+1}))/2$ . *Bottom*: plot as a function of the mean value  $\langle \zeta \rangle_n$ . The colors code the azimuthal orders, as in Fig. 2; the dashed line indicates the 1:1 relation; 1- $\sigma$  uncertainties on both the spacings and the mean values of  $\zeta$  are indicated by vertical and horizontal error bars.

### 3.3. Relationships with $\zeta$

With the identification of the mixed-mode pattern, we aim to verify the relevance of the use of  $\langle \zeta \rangle_n$  for the period spacings, to test the relevance of  $\langle \zeta \rangle_m$  for the rotational splittings, and further test the predictions for the mode widths and heights.

#### 3.3.1. Period spacings

Period spacings were fitted with different functions of  $\zeta$ , according either to the integrated value  $\langle \zeta \rangle_n$  (Eq. 10) or to the arithmetical mean  $\zeta = (\zeta_n + \zeta_{n+1})/2$ . The resulting plots are shown in Fig. 4. When  $\langle \zeta \rangle_n$  is not used, one remarks that the  $\Delta P(\zeta)$  relation shows a modulation that results from the concavity of  $\zeta$ . When  $\zeta$  is close to unity for gravity-dominated mixed modes, no modulation is seen; in the range  $[0.7, 0.9]$ , where the function is convex, the period spacings are larger than predicted; below 0.7, where the function is concave, the period spacings are smaller than expected. The relation between  $\Delta P$  and  $\langle \zeta \rangle_n$  does not show such a modulation. Furthermore, the fit with  $\langle \zeta \rangle_n$  is nearly linear, with residuals two times smaller. From this comparison, we confirm that the use of  $\langle \zeta \rangle_n$  is preferable for fitting the period spacings.

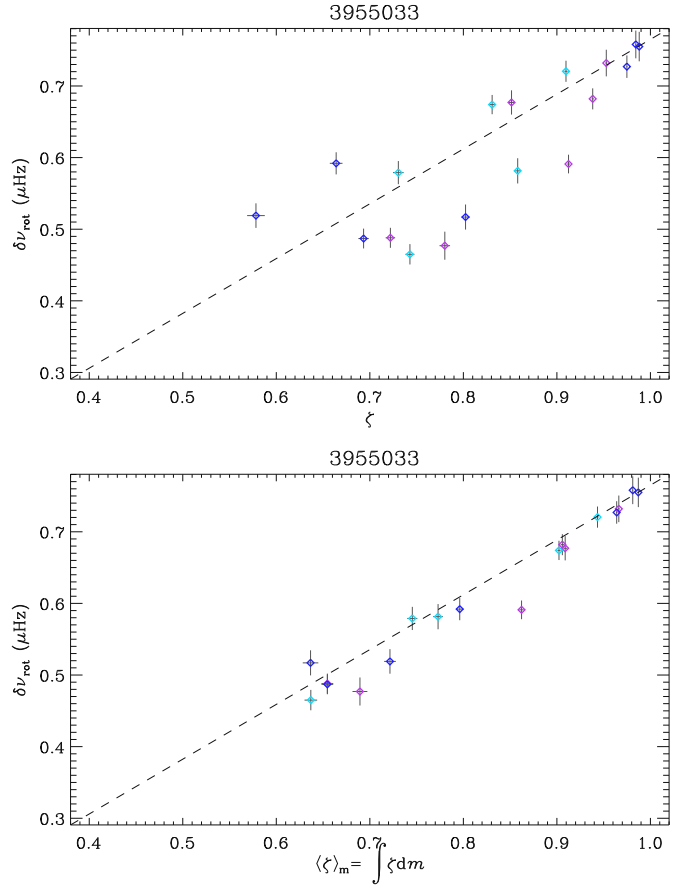


**Fig. 5.** Mean rotation splittings of the RGB star KIC 3955033. *Top*: plot as a function of  $\zeta$ . *Bottom*: plot as a function of the mean value  $\langle \zeta \rangle_m$ . The colors code the azimuthal orders; the dashed line indicates the 1:1 relation; 1- $\sigma$  uncertainties on both the splittings and the mean values of  $\zeta$  are indicated by vertical and horizontal error bars.

#### 3.3.2. Rotational splittings

We performed similar test for the rotational splittings. We a priori excluded a dependence on  $\zeta(\nu_{n,0})$ , since we clearly observe asymmetrical splittings (see below, Section 5.1) that cannot be reproduced with  $\zeta(\nu_{n,0})$ . In fact, the rotation rate of KIC 6144777 is not important enough to observe any difference between the variations with either  $\zeta$  or  $\langle \zeta \rangle_m$ . We therefore performed the fit of the star KIC 3955033 (Fig. A.3), which shows a much more rapid rotation (Fig. 5). From the comparison of  $\delta\nu_{\text{rot}}(\zeta)$  and  $\delta\nu_{\text{rot}}(\langle \zeta \rangle_m)$ , we derive that this latter expression is more convenient since it provides a  $\chi^2$  ten times smaller than when using  $\zeta$ , associated with a much more precise estimate of the core rotation:  $\delta\nu_{\text{rot,core}} = 765 \pm 10$  nHz with  $\langle \zeta \rangle_m$ , versus  $\delta\nu_{\text{rot,core}} = 730 \pm 50$  nHz with  $\zeta$ . From this test, we conclude positively about the relevance of the use of  $\langle \zeta \rangle_m$  for the rotational splittings.

#### 3.3.3. Widths, amplitudes, and heights

As expected from Eq. (19), the mixed-mode width shows large variations: pressure-dominated mixed modes have widths comparable to those of the radial modes, contrary to gravity-dominated modes that are much thinner (Fig. 6, top panel). Figure 6 also shows the validity of Eq. (19), with

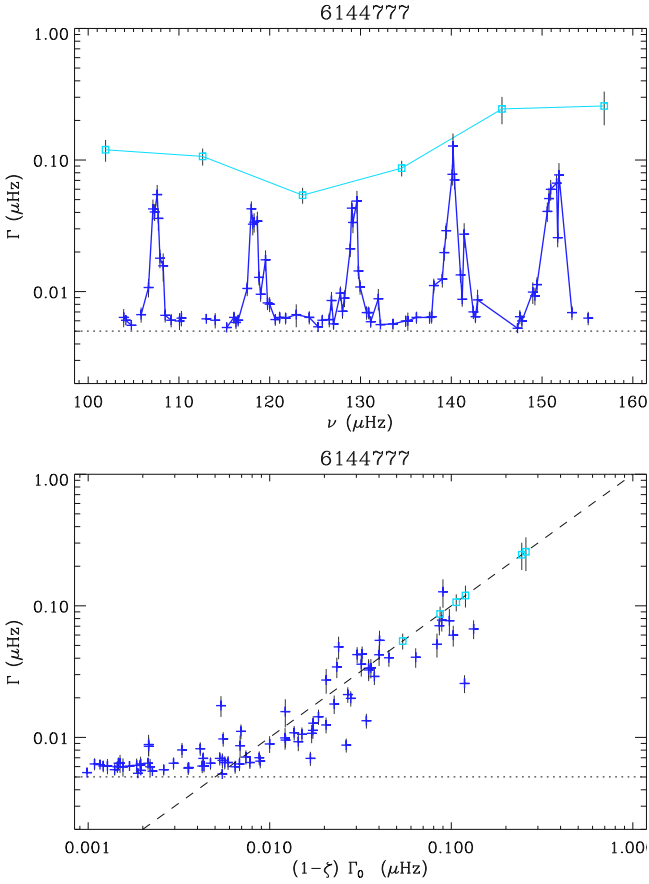


**Fig. 6.** Mode widths as a function of the cyclic frequency (*top*) or as a function of  $(1 - \zeta)\Gamma_0$  (*bottom*), for the RGB star KIC 6144777. Radial modes are plotted with square symbols and dipole mixed modes with +;  $1-\sigma$  uncertainties on  $\Gamma$  are indicated by vertical error bars. The value  $2\delta f_{\text{res}}/\pi$  (Eq. 21) plotted as a dotted line is proportional to the 4-year long frequency resolution. In the bottom plot, radial modes have been considered too, assuming they have  $\zeta = 0$  as pure pressure modes. The dashed line indicates the 1:1 relation.

the mixed-mode width proportional to  $(1 - \zeta)$ , except for low values where the observations resolution hampers the measurement of very thin widths. The precision of the fit is limited by the stochastic excitation, especially for long-lived peaks: the presence or absence of signal in a single frequency bin can modify the width in large proportion. This limit added to the limitation in frequency resolution does not allow us to test if small additional radiative damping affects the gravity-dominated mixed modes (Dupret et al. 2009; Grosjean et al. 2014).

As shown by Mosser et al. (2015), Eq. (20) has a strong theoretical justification, since it expresses the conservation of energy: the sum of all the energy distributed in the mixed modes corresponds to the energy expected in the single pure pressure mode that should exist in absence of any coupling. So, our result is in line with the findings of Mosser et al. (2012a), who measured that, except for depressed modes, the observed total visibility of dipole modes matches the theoretical expectations.

Due to the stochastic nature of the excitation, the mode heights show a large spread (Fig. 7). Dips in the distributions occur when modes are not resolved. It is however clear in Fig. 7 bottom that the dipole mode heights follow the

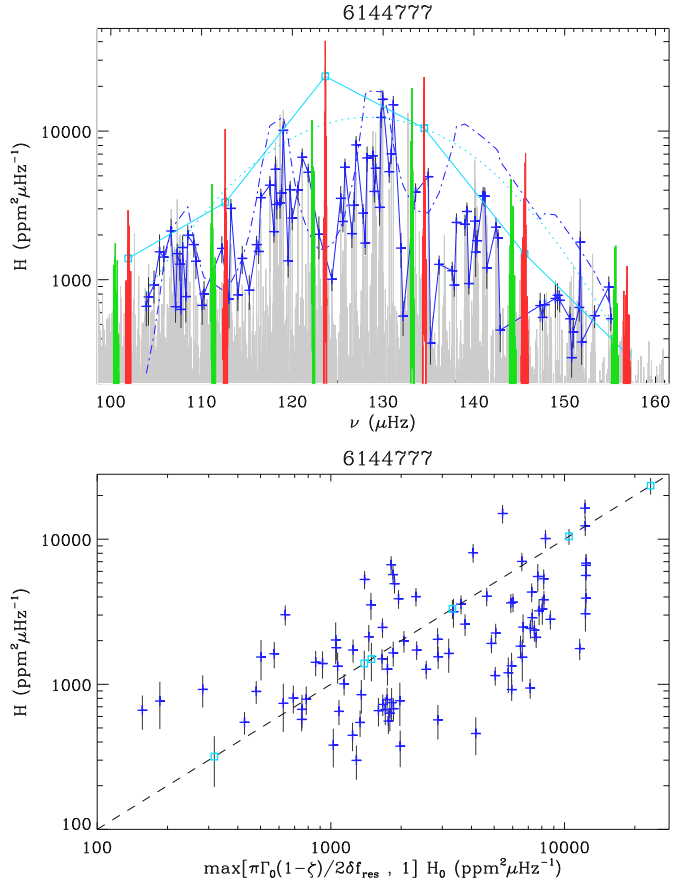


**Fig. 7.** Mode heights as a function of the cyclic frequency (*top*) or as a function of the radial mode height, modified when the modes are not resolved, (*bottom*), for the RGB star KIC 6144777. Radial modes are plotted with square symbols and dipole mixed modes with +. The Fourier spectrum is plotted in red (green) for emphasizing the radial (quadrupole) modes. The dot-dashed line provides the expected heights of dipole modes, under the assumption that the power excess mimics a Gaussian relation (dotted line). The dashed line indicates the 1:1 relation.

radial distribution according to the trend of Eq. (21). We note that all mixed modes associated with a given pressure radial order show a systematic behavior. For instance, all mixed modes of KIC 6144777 in the frequency range  $[137, 143 \mu\text{Hz}]$  associated with the pressure mode  $n_p = 11$  show lower amplitudes than expected from the Gaussian fit of the power excess. Such a behavior recalls us that the excitation of a mixed mode is due to its acoustic component.

### 3.4. Validation

From these two case studies and from other examples shown in Appendix, we can conclude that the asymptotic fits are relevant at all evolutionary stages, when the signal-to-noise ratio is high enough. So, the equations developed in Section 2 allow us to depict the mixed-mode spectrum with a very high accuracy, when the integrated values  $\langle \zeta \rangle_n$  and  $\langle \zeta \rangle_m$  are considered for the period spacings and the rotational splittings, respectively. Up to now, only red clump stars showing buoyancy glitches cannot be fitted with a single set of parameters.



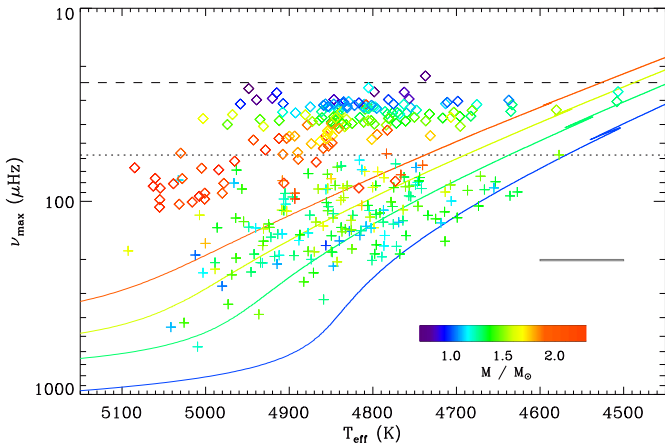


**Fig. 8.** Seismic diagram of the 372 red giants studied in this work, with  $\nu_{\max}^{-1}$  used as a proxy for the luminosity. The color codes the stellar mass. Stars on the RGB are plotted with + symbols, red clump stars with  $\diamond$ . The dotted and dashed lines indicate the limit of the visibility of mixed modes for RGB and clump stars, respectively, as defined by Eq. (31). Evolution tracks on the RGB, computed with MESA for solar metallicity (Gehan et al. 2018), are shown for the stellar masses 1.0, 1.3, 1.6, and 1.9  $M_{\odot}$ . The error box indicates the typical 1- $\sigma$  uncertainties on  $T_{\text{eff}}$  and  $\nu_{\max}$ .

#### 4. Asymptotic period spacings and gravity offsets

In this section, we show how previous findings can be used to derive accurate period spacings. We also explore the variation of the gravity offsets  $\varepsilon_g$  with stellar evolution. These studies rely on the determination of the pure-gravity mode pattern.

##### 4.1. Observations

Our analysis was conducted over 372 red giants at various evolutionary stages, mainly from Mosser et al. (2014) and Vrad et al. (2016), with stars also considered in Beck et al. (2012), Kallinger et al. (2012), Deheuvels et al. (2014), and Corsaro et al. (2015). Data were obtained as for the two stars considered in Section 3. When available, effective temperatures are from APOGEE spectra (Albaret et al. 2017). Selection criteria are mainly based upon the noise level, with *Kepler* magnitudes brighter than 12 on the low RGB or 14 for more evolved stars. Following the method exposed in Section 3.1, we need data with a S/R high enough to allow the identification of gravity-dominated mixed modes. When such modes are too few, measurements are impossible. This condition induces a selection bias, specifically addressed in Section 6.

The 372 stars that were analyzed are shown in a seismic diagram (Fig. 8). We considered stars from the low RGB (Fig. A.1) to more evolved RGB stars (Fig. A.2). The spectrum of the evolved RGB star KIC 2443903 (Fig. A.4) corresponds to a case near the limit of visibility of gravity-dominated mixed modes, with a mode density  $\mathcal{N} \simeq 22.4$  close to the limit value above which the detection is impossible (Section 6). The fitting process for red clump stars can be achieved only when the amplitude of the buoyancy glitches remains limited (Fig. A.5); the same limitation appears in the secondary red clump (Fig. A.6). In fact, except for red-clump stars with large buoyancy glitches (Cunha et al. 2015; Mosser et al. 2015), the asymptotic expansion

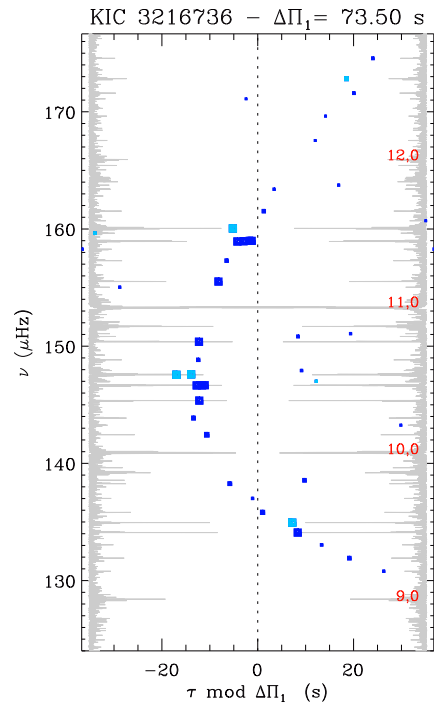


**Fig. 9.** Stretched-period échelle diagram of KIC 3216736, the only RGB star in our sample showing buoyancy glitches. The spectrum is simple, since only  $m = 0$  dipole mixed modes are present, but shows a large-period modulation instead of the expected vertical alignment. Modes plotted in light blue are pressure dominated; extra peaks that do not follow the global trend are either  $\ell = 3$  modes or  $\ell = 2$  mixed modes. Red figures indicate the radial orders of the radial modes. For clarity, the power spectrum density is also plotted twice, top to tail.

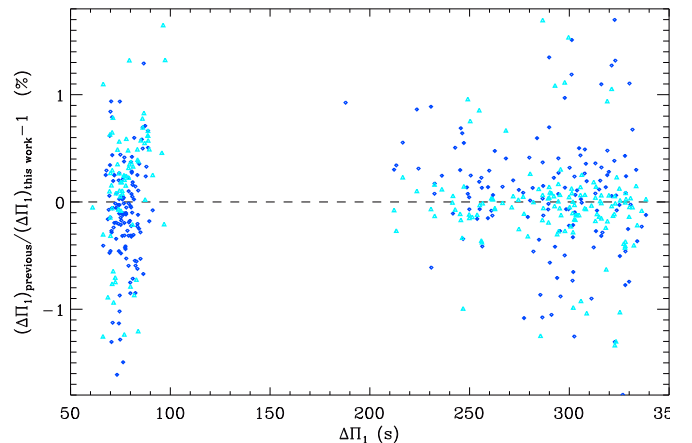


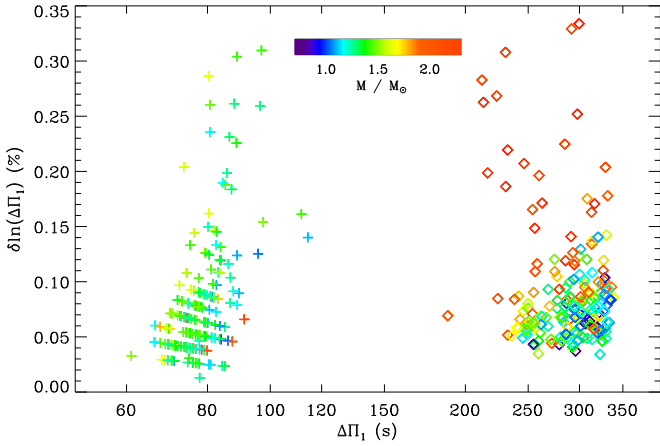
**Fig. 10.** Comparison of the asymptotic period spacings with previous values. Light blue triangles show the bias in period spacings computed under the assumption  $\varepsilon_g = 0$  (Mosser et al. 2014), whereas dark blue diamonds are free of this hypothesis (Vrad et al. 2016).

provides a relevant fit. We could then obtain precise measurements of the asymptotic gravity parameters in Eq. (4) and of their uncertainties for a large number of stars. We must report one exception: KIC 3216736 is the only RGB star of our sample where we found buoyancy glitches and could not provide a relevant fit of the spectrum, but only an échelle diagram based on stretched periods (Fig. 9). Since

**Table 1.** Period spacings and gravity offsets

KIC	$\nu_{\max}$ ( $\mu\text{Hz}$ )	$\Delta\nu$ ( $\mu\text{Hz}$ )	$\Delta\Pi_1$ (s)	$q$	$\varepsilon_g$	$\delta\nu_{\text{rot}}$ (nHz)
1576469	$90.60 \pm 0.98$	$7.41 \pm 0.04$	$284.80 \pm 0.64$	$0.23 \pm 0.03$	$-0.102 \pm 0.096$	$67 \pm 6$
1723700	$39.42 \pm 0.57$	$4.48 \pm 0.04$	$323.40 \pm 0.17$	$0.24 \pm 0.04$	$0.066 \pm 0.043$	$57 \pm 5$
2437976	$89.37 \pm 1.10$	$8.22 \pm 0.05$	$74.70 \pm 1.00$	$0.10 \pm 0.02$	$-0.006 \pm 0.095$	$320 \pm 30$
2443903	$66.76 \pm 0.90$	$7.01 \pm 0.04$	$71.10 \pm 0.02$	$0.12 \pm 0.02$	$-0.184 \pm 0.078$	$360 \pm 4$
3955033	$106.10 \pm 1.24$	$9.23 \pm 0.05$	$74.65 \pm 0.06$	$0.13 \pm 0.02$	$0.207 \pm 0.115$	$765 \pm 10$
5024476	$68.66 \pm 0.75$	$5.73 \pm 0.04$	$299.60 \pm 1.00$	$0.27 \pm 0.03$	$-0.199 \pm 0.102$	$63 \pm 6$
5112373	$43.82 \pm 0.59$	$4.63 \pm 0.04$	$240.30 \pm 0.14$	$0.19 \pm 0.02$	$-0.246 \pm 0.058$	$37 \pm 3$
6144777	$128.23 \pm 1.50$	$11.03 \pm 0.05$	$79.05 \pm 0.04$	$0.13 \pm 0.02$	$0.210 \pm 0.055$	$244 \pm 5$
10272858	$341.45 \pm 6.16$	$22.71 \pm 0.14$	$96.90 \pm 0.30$	$0.19 \pm 0.02$	$0.338 \pm 0.098$	$660 \pm 20$
11353313	$127.29 \pm 1.46$	$10.75 \pm 0.05$	$76.95 \pm 0.06$	$0.14 \pm 0.02$	$0.290 \pm 0.088$	$465 \pm 7$

The list of the full data set with 372 red giants showing an uncertainty in  $\varepsilon_g$  less than 0.15 is available on line as a CDS/VizieR document.


**Fig. 11.** Relative precision of the asymptotic period spacings. Same style as in Fig. 8.

we have tested more than 160 stars on the RGB, with a systematic approach, we can conclude that the most common case on the RGB is the absence of buoyancy glitches, as expected theoretically (Cunha et al. 2015).

Characterizing the sample we studied in terms of bias is difficult. Apart from the RGB stars that were already studied in detail in previous works, we have mostly treated the stars with increasing KIC numbers. This systematic method implies that we did not introduce any further bias compared to the *Kepler* sample of red giants. Considering a high enough S/R, which is almost equivalent to select bright stars in the red giant domain, is not supposed to introduce biases either. Contrary to many previous studies, we are not limited to stars showing rotational splittings smaller than the confusion limit ( $\delta\nu_{\text{rot}} \leq \nu_{\text{max}}^2 \Delta\Pi_1$ ). However, the presence of a strong cutoff (Section 6) limits the sample, when gravity-dominated mixed modes disappear. Red-clump stars with strong buoyancy glitches are absent in our data set since the fitting process requires then to account for the extra-modulation, which can be quite large (about  $\Delta\Pi_1/10$ ). When mixed modes are depressed, the low height-to-background ratio of the mixed modes allows the measurement of  $\Delta\Pi_1$  (Mosser et al. 2017a) but is not enough for fitting the pattern. Both cases deserve specific care beyond the scope of this work.

#### 4.2. Pure gravity modes

The identification of the mixed modes depicted in Section 3.1 allows us to retrieve the periods of the pure gravity modes and to infer global asymptotic parameters of the gravity components. We compute these periods from the mixed-mode frequencies  $\nu$ , using Eqs. (1) and (2),

$$\frac{1}{\nu_g} = \frac{1}{\nu} - \frac{\Delta\Pi_1}{\pi} \operatorname{atan} \left( \frac{\tan \theta_p}{q} \right). \quad (25)$$

Close to each radial mode, when  $\theta_p$  varies from values less than but close to  $\pi/2$  to values higher than but close to  $-\pi/2$ , the atan correcting term introduces an offset of  $-\Delta\Pi_1$ , which in fact allows to relate the  $(\mathcal{N} + 1)$  mixed modes in the  $\Delta\nu$ -wide interval to  $\mathcal{N}$  only gravity modes. In order to use all mixed modes, including the  $|m| = 1$  components, we corrected first the rotational splittings, using Eq. (16) in order to obtain  $\nu$  values that are corrected from the rotational splitting.

From the periods of the gravity modes  $1/\nu_g$ , we could then derive the asymptotic parameters  $\Delta\Pi_1$  and  $\varepsilon_g$ , assuming the first-order asymptotic expression for pure gravity modes (Eq. 4). In practice, a first estimate of  $\Delta\Pi_1$  derived from the formalism of Mosser et al. (2015) and Vrad et al. (2016) is used in Eq. (25), then iterated with a least-square fit of the linear variation of the gravity modes (Eq. 4).

#### 4.3. Asymptotic period spacings

Up to now, measurements of  $\Delta\Pi_1$  considering that  $\varepsilon_g$  is a free parameter have been obtained for a few stars only (Buyschaert et al. 2016; Hekker et al. 2018, for 3 and 22 observed stars, respectively). The offset  $\varepsilon_g$  being arbitrarily fixed, Mosser et al. (2012b) and Mosser et al. (2014) reported a very high precision for the period spacings, of typically 0.1s for stars on the RGB and 0.3s in the red clump. However, owing to the choice of  $\varepsilon_g = 0$ , their period spacings were slightly affected by a bias of about a fraction of  $\nu_{\text{max}} \Delta\Pi_1^2$ . The values reported by Vrad et al. (2016), free of any hypothesis on  $\varepsilon_g$ , are not biased but show uncertainties typically five to fifteen times higher than the new values. Their comparison with our data confirms the absence of systematic offsets (Fig. 10). So, the new method ensures accuracy, in the sense that the measurements of  $\Delta\Pi_1$  are now free of any hypothesis on  $\varepsilon_g$  and prove that the asymptotic expansion for gravity modes (Eq. 4) is relevant. The relative accuracy we obtained for the period

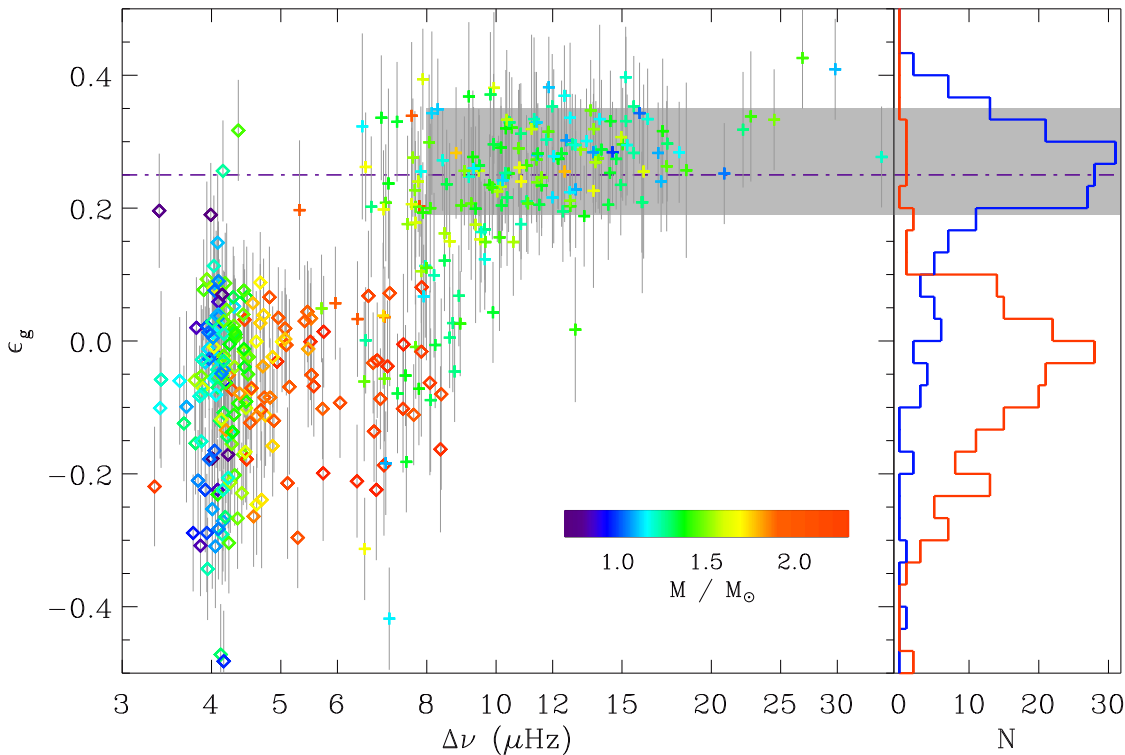


**Fig. 12.** *Left:* variation of  $\varepsilon_g$  with  $\Delta\nu$ , with the same style as Fig. 11. The horizontal dark gray domain corresponds to the expected range predicted for RGB stars by Takata (2016a), whereas the dot-dashed line shows the value  $\varepsilon_{g,as} = 1/4$  derived from the asymptotic expansion (Provost & Berthomieu 1986). Uncertainties on  $\varepsilon_g$  are indicated by vertical lines; uncertainties on  $\Delta\nu$  are smaller than the symbol size. *Right:* histograms of the distributions of  $\varepsilon_g$  on the RGB (blue curve) and in the red clump (red curve). The dot-dashed line and the gray domain have the same meaning as indicated above.

spacings, assuming Eq. (4), is shown in Fig. 11. The median relative accuracies on the RGB and in the red clump are similar, of about  $7 \cdot 10^{-4}$ . They translate, respectively, into 0.06 s on the RGB and 0.22 s in the red clump; Hekker et al. (2018) reach a similar precision.

#### 4.4. Gravity offsets $\varepsilon_g$

We could measure  $\varepsilon_g$  for a large set of stars. We however have to face the indetermination of  $\varepsilon_g$  modulo 1: we simply assume that  $\varepsilon_g$  is in the range  $[-0.5, 0.5]$ . The  $\varepsilon_g$  values computed for the set of stars presented in the paper is given in Table 1 and plotted in Fig. 12, where an histogram is also given. The complete table is given online only. Uncertainties on  $\varepsilon_g$  are small, related to the uncertainties in  $\Delta\Pi_1$  by

$$\delta\varepsilon_g = \frac{\delta\Delta\Pi_1}{\nu_{\max} \Delta\Pi_1^2}. \quad (26)$$

This relation comes from the derivative of Eq. (4). As a result, the median uncertainties are of about 0.08 on the RGB and 0.06 in the red clump.

We noticed that the median value of  $\varepsilon_g$  on the RGB is in fact close to  $1/4$ , which is the expected asymptotic value in absence of stratification below the convection zone (Provost & Berthomieu 1986), derived from the contribution  $\ell/2 - \varepsilon_{as}$  with  $\ell = 1$  and  $\varepsilon_{as} = 1/4$ . Hence, we inferred that the degeneracy on the determination of  $\varepsilon_g$  is removed. We then noted a slight decrease in  $\varepsilon_g$  when stars evolve on the RGB, with an accumulation of values close to 0 for red-clump stars. Hekker et al. (2018) reported values of  $\varepsilon_g$  in the range  $[-0.2, 0.5]$  for 21 stars on the RGB, but did not

identify the accumulation of values in the range  $[0.20, 0.35]$  predicted by Takata (2016a) for stars on the low RGB. Our measurements fully confirm this prediction. From a check of their data set, we interpret the differences in  $\varepsilon_g$  as resulting from less precise gravity spacings when large rotational splittings apparently modify the period spacings. As made clear by the recent theoretical developments of the asymptotic expansion (Takata 2016b,a), the accurate measurement of the leading-order term  $\Delta\Pi_1$  is necessary to provide reliable estimates of  $\varepsilon_g$ .

We can study the variation of  $\varepsilon_g$  along stellar evolution. On the RGB, the asymptotic expansion predicts  $\varepsilon_g = 1/4 - \vartheta$  (Provost & Berthomieu 1986), where  $\vartheta$  is a measure of the stratification just below the convection zone. From this dependence, we can infer that the term  $\vartheta$  is certainly very small for most stars on the low RGB. Higher values are suspected for evolved RGB stars, but with too few stars to firmly conclude, whereas lower values are seen for evolved RGB. We checked that the change of regime of  $\varepsilon_g$  is not associated with the luminosity bump since it occurs for more evolved stars than our sample (Khan et al. 2018). In the red clump, the  $\vartheta$  correction seems important, on the order of 0.3, with a larger spread than observed on the RGB.

An extended study of  $\varepsilon_g$  can now be performed to use this parameter as a probe of the stratification occurring in the radiative region. This study is however beyond the scope of this work.

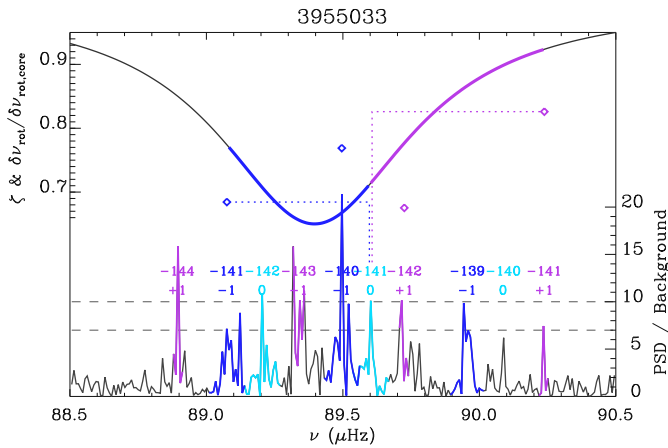


**Fig. 13.** Splitting asymmetry at low frequency in KIC 3955033. Each dipole mixed mode of the spectrum is labelled with its radial and azimuthal orders. The rotational splittings of the radial orders from  $-142$  to  $-140$ , plotted with diamonds, do not match the function  $\zeta$ . Only the multiplet with  $n = -141$  is complete: the  $m = +1$  splitting is much larger than the  $m = -1$  splitting; the colored regions indicate the ranges over which the function  $\zeta$  is integrated for the components of the multiplet  $n = -141$ . The dashed lines indicate height-to-background values of 7 and 10.

## 5. Rotation

The fits based on the function  $\zeta$  also allow us to analyze rotational splittings in detail.

### 5.1. Splitting asymmetry

Recently, asymmetries in the rotational splittings were reported by Deheuvels et al. (2017), as the signature of the combined effects of rotation and mode mixing. Using both perturbative and non-perturbative approaches, they computed near-degeneracy effects and could fit the data. In fact, the asymptotic development of mixed modes also describes the combined effects of rotation and mode mixing, so that the rotational splittings based on  $\langle \zeta \rangle_m$  (Eqs. 16 and 18) are not symmetric. Inversely, the symmetrical rotational splitting based on  $\zeta$  (Eq. 15) does not reproduce the observed asymmetry. Hence, observing asymmetrical triplets is a way to prove the relevance of the use of  $\langle \zeta \rangle_m$  instead of  $\zeta$ .

Observing the asymmetry is challenging but possible for stars with a rapid rotation rate. As explained by Gehan et al. (2017, 2018), rapid rotation means  $\delta\nu_{\text{rot}} \geq \Delta\nu/\mathcal{N}$  for seismology. This rotation is however very slow in terms of interior structure, so that the formalism developed by Goupil et al. (2013) and Deheuvels et al. (2014), summarized by Eq. (16), remains relevant. It simplifies the study, as shown by Ouazzani et al. (2013) who treated the case where rotational splittings can be as large as  $\Delta\nu$ . We fitted the mixed-mode spectrum of KIC 3955033 with both the symmetrical and asymmetrical splitting. At high radial order  $n_p$ , it is hard to distinguish them. At low orders, when the rotational splittings exceed the mixed-mode spacings, the symmetrical splittings fail whereas the asymmetrical one provides a consistent solution along the whole spectrum. The radial order  $n_p = 8$  is shown in Fig. 13, the whole spectrum is shown in Fig. A.3.

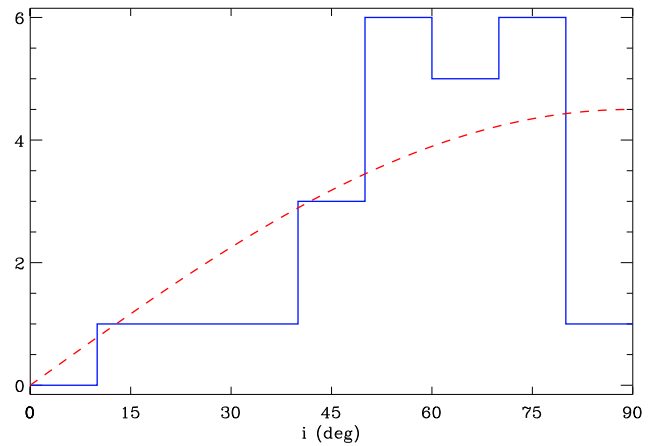


**Fig. 14.** Histogram of the inclinations measured in NGC 6819. The dashed line indicates the  $\sin i$  distribution.

### 5.2. Surface rotation

For stars on the low RGB, surface rotation can be inferred from the rotational splittings (Eq. 15). The measurement is however difficult, since it results from an extrapolation at  $\zeta = 0$ , when values are mostly obtained above  $\zeta = 0.6$  only (Fig. 5). The highest level of precision, hence the use of  $\langle \zeta \rangle_m$  instead of  $\zeta$ , is required for deriving a correct estimate of the surface rotation. The case of KIC 3955033 is illustrative, with a negative surface rotation when using  $\zeta$ ; the use of  $\langle \zeta \rangle_m$  provides a null value ( $5 \pm 20$  nHz). This case also confirms the general situation shown by previous works (Goupil et al. 2013; Di Mauro et al. 2016; Triana et al. 2017): deriving surface rotation can be achieved for the low RGB only.

### 5.3. Stellar inclination

From its ability to fit the gravity-dominated modes that carry useful information, the asymptotic fit can be used to derive the stellar inclination  $i$ . The amplitude of the  $m = 0$  component of the dipole multiplet is proportional to  $\sin^2 i$  whereas the sum of the amplitudes of the  $m = \pm 1$  mode is proportional to  $\cos^2 i$ . From Eq. (20), a correction factor of  $1/(1 - \zeta)$  should be applied on the amplitudes: its differential effect is however much below the precision one can get on  $i$ .

We tested our results on a set of stars for which the inclinations measured with other methods have been obtained. We checked that our results are relevant, with a precision limited by the uncertainties on the amplitude measurements. In order to avoid bias, we consider only peaks with a height-to-background ratio larger than 8. Nevertheless, we noted that the stochastic excitation of the modes induces a small bias for large inclinations. Equator-on inclinations, near  $90^\circ$ , cannot be retrieved precisely, with measurements reduced toward the range  $70$ – $80^\circ$ . As a consequence, they are rare in our analysis. However, many stars show inclinations that, according to the uncertainties, are compatible with equator-on measurement, so that the bias does not affect the following analysis.

We measured inclinations of red giants in the open clusters NGC 6819 observed by *Kepler* (e.g., Basu et al. 2011; Stello et al. 2011; Miglio et al. 2012). We selected the stars that exhibit mixed modes and could fit 20 mixed-mode

**Table 2.** Asymptotic and rotational parameters in NGC 6819

KIC ID	$\Delta\nu$ ( $\mu\text{Hz}$ )	$\Delta\Pi_1$ (s)	$q$	$\delta\nu_{\text{rot}}$ (nHz)	$i$ ( $^\circ$ )
4937056	4.76	291.0	0.21	90	$60\pm 15$
4937257 <sup>a</sup>	4.13	292.1	0.19	27	$72\pm 13$
4937770 <sup>b</sup>	7.82	161.0	0.18	×	×
4937775 <sup>a</sup>	7.33	226.3	0.21	110	$75\pm 15$
5023953	4.74	293.9	0.24	50	$51\pm 28$
5024327	4.72	269.5	0.20	55	$56\pm 13$
5024404	4.78	242.6	0.25	110	$80\pm 10$
5024414	6.47	283.0	0.30	90	$45\pm 20$
5024476	5.73	299.5	0.24	56	$71\pm 11$
5024582	4.76	323.5	0.22	70	$55\pm 18$
5111718	10.59	88.4	0.12	410	$69\pm 21$
5111949	4.81	319.0	0.28	35	$66\pm 15$
5112072	10.08	91.9	0.15	350	$72\pm 12$
5112361 <sup>c</sup>	6.19	99.0	0.12	350	$70\pm 20$
5112373	4.63	240.2	0.19	37	$47\pm 18$
5112387	4.70	267.2	0.28	84	$25\pm 17$
5112401	4.03	311.0	0.26	50	$54\pm 13$
5112467	4.75	285.2	0.25	90	$61\pm 12$
5112491	4.68	324.3	0.30	150	$31\pm 16$
5112730	4.56	320.0	0.25	45	$56\pm 18$
5112938	4.73	320.0	0.30	65	$45\pm 11$
5112950	4.35	319.5	0.38	38	$61\pm 18$
5112974	4.32	309.6	0.24	60	$50\pm 12$
5113441 <sup>c</sup>	11.75	89.0	0.13	730	$18\pm 18$
5200152	4.73	327.2	0.28	50	$70\pm 15$

<sup>a</sup>: KIC 4937257 and KIC 4937775 are absent in Corsaro et al. (2017).

<sup>b</sup>: × symbols indicate the absence of any reliable asymptotic fit for KIC 4937770.

<sup>c</sup>: Different solutions in  $\Delta\Pi_1$  are possible for KIC 5112361, which all provide a high inclination. Different solutions in  $\delta\nu_{\text{rot}}$  are possible for KIC 5113441, which all provide a low inclination.

Typical uncertainties for those stars with low S/R spectra are 0.7% in  $\Delta\nu$  and  $\Delta\Pi_1$ , 12% in  $q$ , and 8% in  $\delta\nu_{\text{rot}}$ .

patterns with the asymptotic expansion. In one case, the asymptotic fit is impossible, due to a low S/R. In two other cases, different possible solutions exist, based either on different period spacings, or on different rotational splittings, but without any ambiguity for the inclination measurement: when two peaks dominate per period spacing, the inclination is necessarily high, whereas it is low when one single peak only is present. We completed this list with other NGC 6819 members listed in Handberg et al. (2017) and could fit two additional stars, which incidentally show a large inclination. Results for the inclinations and rotational splittings are given in Table 2. As shown in Fig. 14, the distribution of the stellar inclinations mimics the  $\sin i$  relation expected for random inclinations, except near  $90^\circ$ , due to bias mentioned above. A similar test performed on the open cluster NGC 6791 reaches the same conclusion.

Low stellar inclinations in NGC 6819 and 6791 were measured by Corsaro et al. (2017), using a Bayesian analysis, from which aligned spins were inferred. Our measurements however contradict their claim, as shown in Fig. 15 for NGC 6819. In fact, our measurements compared to theirs agree for high inclinations, whereas they mostly disagree for low inclinations. Comparison with the asymptotic fits shows that their Bayesian rotational splittings are most often overestimated and that the related inclinations are most often underestimated.

In fact, the asymptotic fit can be used as a prior for the Bayesian fit. It indicates that the rotational splitting is derived from the thin gravity-dominated mixed modes, with

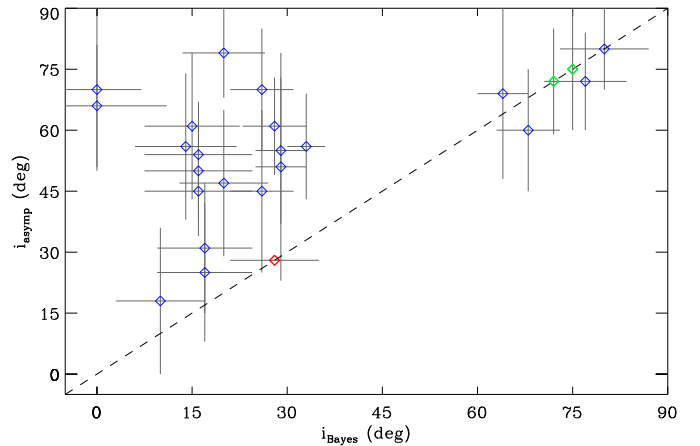


**Fig. 15.** Comparison of the inclinations of the spin axis of the stars in NGC 6819. Inclinations measured by Corsaro et al. (2017) are plotted on the x-axis, while inclinations derived from the asymptotic analysis are on the y-axis;  $1\text{-}\sigma$  uncertainties are indicated by vertical and horizontal error bars. The red symbol shows the case where no asymptotic fit could be found, and the green ones to cases without Bayesian fit. The dashed line corresponds to the 1:1 relation.

narrow widths (Eq. 19) and average rotational splittings slightly inferior to the mean core rotation  $\delta\nu_{\text{rot}}$  (Eq. 16). Mixed modes at low pressure radial orders, with frequencies much below  $\nu_{\text{max}}$ , are especially informative, since previous work has shown that their radial mode widths, hence their mixed-mode widths according to Eq. (19), are the thinnest possible (Fig. 5 of Vrad et al. 2018). Figure 1 of the supplementary material of Corsaro et al. (2017) provides an explanation of the discrepant Bayesian values. Their fit of the star KIC 5112373 in NGC 6819 provides nearly uniform large mode widths, relevant for the pressure-dominated mixed modes but much too high for gravity-dominated modes, in contradiction with the physical variation indicated by Eq. (19). As a consequence, their fit assumes that all the power is concentrated in the  $m = 0$  mode; the resulting stellar inclination is  $20 \pm 8^\circ$ . We show the asymptotic solution of KIC 5112373 in Fig. 16, with thin gravity dominated mixed modes and the clear identification of triplets. Since  $m = \pm 1$  modes are observed all along the spectrum, our solution for the inclination is larger, about  $47 \pm 18^\circ$ .

We provide another example with the star KIC 2437976, a NGC 6791 member. As shown in Fig. 17, rotational splittings are explained in a consistent way with thin unresolved gravity-dominated mixed modes and a rotation rate rapid enough to ensure that close modes *do not* belong to the same multiplets. All peaks can be explained by the  $m = \pm 1$  modes. In practice,  $m = 0$  modes are absent, so that this star has necessarily an inclination close to  $90^\circ$ , whereas Corsaro et al. (2017) measured  $i \simeq 0^\circ$ . We conclude that some of the low inclinations reported in Corsaro et al. (2017) are incompatible with the analysis presented here. It seems that the difference is due to a too low range of the linewidth priors in the Bayesian analysis, which favors a solution with a low inclination angle and a high splitting. As a result, stellar spins in old open clusters are neither aligned nor quasi parallel to the line of sight. Our study emphasizes a major role for the asymptotic analysis: pro-

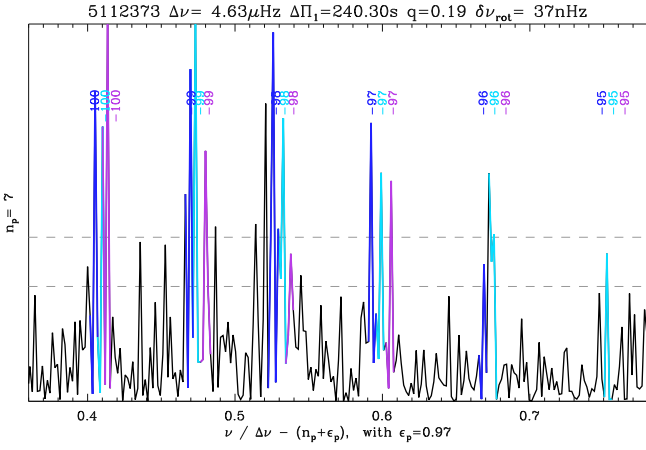


**Fig. 16.** Fit of the mixed modes corresponding to  $n_p = 7$  in KIC 5112373 (NGC 6819 member). The color codes the azimuthal order:  $m = +1$  in purple,  $m = -1$  in blue. The gray dashed lines indicate the two thresholds used in this work, corresponding to height-to-background ratios of 7 and 10. Contrary to the analysis conducted by Corsaro et al. (2017), modes with  $m = \pm 1$  are clearly identified.

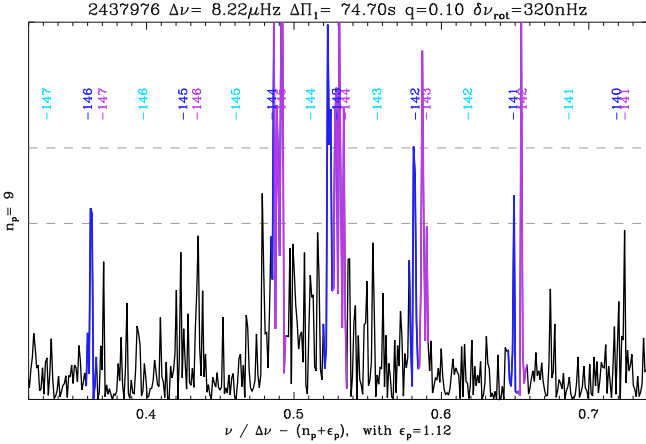


**Fig. 17.** Fit of the mixed modes corresponding to  $n_p = 9$  in KIC 2437976 (NGC 6791 member). The color codes the azimuthal order:  $m = +1$  in purple,  $m = -1$  in blue. The location of  $m = 0$  modes is indicated in light blue, but none shows a large height for this star seen equator-on. The gray dashed lines indicate the two thresholds used in this work, corresponding to height-to-background ratios of 7 and 10. Many peaks above the threshold value 5.5 that rejects the null hypothesis at the 5%-level follow the mixed-mode pattern.

viding relevant estimates of all features of the mixed-mode pattern, including mode widths.

## 6. Observability of the mixed modes

All the information derived from mixed modes relies on their observability. The properties of the function  $\zeta$  can be used to assess under which conditions mixed modes can be actually observed. To achieve this, we investigate first the domain where pressure-dominated mixed modes are observed, then the condition for observing gravity-dominated mixed modes.

### 6.1. Pressure-dominated mixed modes

We can define the frequency range where mixed modes are pressure-dominated (pm) from the full width at half minimum of the  $\zeta$  function. So, these modes cover a range, expressed in terms of the pressure phase  $\theta_p$  (Eq. 6), verifying

$$\delta\theta_p|_{\text{pm}} = 2q \sqrt{1 + \frac{1}{\mathcal{N}q}} \quad (27)$$

under the assumption that  $q$  is small, which is verified for all stars except at the transition between subgiants and red giants (Mosser et al. 2017b). When expressed in frequency and compared to the large separation, this condition corresponds to a frequency range surrounding each pure pressure modes with a width  $\delta\nu_{\text{pm}}$  defined by

$$\frac{\delta\nu_{\text{pm}}}{\Delta\nu} = \frac{2q}{\pi} \sqrt{1 + \frac{1}{\mathcal{N}q}}. \quad (28)$$

The variations in  $q$  and  $\mathcal{N}$  explain the narrowing of the region with pressure-dominated mixed modes when stars evolve on the RGB. An example is shown in the Appendix (Fig. A.4). The expression of  $\delta\nu_{\text{pm}}$  also shows that red-clump stars, with larger  $q$  show pressure-dominated mixed modes in a broader region than RGB stars.

### 6.2. Visible gravity-dominated mixed modes

The non-dilution of the mode height expressed by Eq. 21 can be used to define a criterion of visibility of the gravity-dominated (gm) mixed modes. So, they are clearly visible when they show heights similar to those of the pressure modes ( $H_n = H_0$ ), hence when  $\Gamma_0(1 - \zeta) \geq 2\delta f_{\text{res}}/\pi$  (Eq. 19). This condition translates into

$$(1 - q^2) \sin^2 \theta_p \leq \frac{q}{\mathcal{N}} \left( \frac{\pi}{2} \frac{\Gamma_0}{\delta f_{\text{res}}} - 1 \right) - q^2. \quad (29)$$

Except at the transition from subgiants to red giants, where mixed modes are unambiguously visible (Benomar et al. 2013; Deheuvels et al. 2014), the terms  $q^2$  are negligible, so that modes are clearly visible if

$$|\sin \theta_p|_{\text{gm}} \leq \sqrt{\frac{q}{\mathcal{N}} \left( \frac{\pi}{2} \frac{\Gamma_0}{\delta f_{\text{res}}} - 1 \right)}. \quad (30)$$

This condition for observing gravity-dominated mixed modes has many consequences:

- It can be fulfilled only if the definition of the right term is ensured, which requires a frequency resolution low enough compared to the radial mode width. With  $\Gamma_0$  in the range [100, 150 nHz], the observation must last 50-75 days at least. In fact, mixed modes were observable with CoRoT runs lasting about 150 days (Mosser et al. 2011a), but are hardly observable with K2 80-day time series (Stello et al. 2017).
- When stars evolve on the RGB, the decrease in  $q$  and increase in  $\mathcal{N}$  contribute to the narrowing of observable modes. Mixed modes are more easily visible in the red clump, owing to larger  $q$  values. This criterion is implicitly used by Elsworth et al. (2017) for their determination of the evolutionary state of red-giant stars.
- All mixed modes are clearly visible when the condition expressed by Eq. (30) is always met, that is when

$\mathcal{N} \leq q(\pi\Gamma_0/2\delta f_{\text{res}} - 1)$ . This condition is met for subgiants, on the lower RGB, and for secondary-clump stars (Mosser et al. 2014).

- No mixed mode can be observed when the condition is so drastic that only pressure-dominated mixed modes can be observed. The combination of the conditions expressed by Eq. (27) and Eq. (30) yields the limit of visibility of gravity-dominated mixed modes, expressed by a condition on the mixed-mode density

$$\mathcal{N} \leq \frac{1}{4q} \left( \frac{\pi}{2} \frac{\Gamma_0}{\delta f_{\text{res}}} - 5 \right). \quad (31)$$

In the conditions of observation of *Kepler*, with typical parameters defined as in Mosser et al. (2017a), this limit corresponds to a mode density  $\mathcal{N}$  of about 25, for RGB and clump stars, over which no gravity-dominated mixed modes can be identified. This theoretical estimate is observed in practice, with a few exceptions with larger  $\mathcal{N}$  (Fig. 8). On the RGB, observation of mixed modes with *Kepler* is limited to  $\Delta\nu \geq 6 \mu\text{Hz}$ , whereas the limit is around  $3 \mu\text{Hz}$  for clump stars. As a consequence, visible mixed modes in an oscillation spectrum with  $\Delta\nu$  in the range  $[3, 6 \mu\text{Hz}]$  most often indicate a red-clump star. Incidentally, the location of the RGB bump was recently identified by Khan et al. (2018) in the range  $[5, 6 \mu\text{Hz}]$ , depending on the stellar mass and metallicity. This means that sounding the bump with mixed modes will be very difficult, if not impossible.

## 7. Conclusion

The asymptotic analysis allows us to depict the whole properties of the mixed-mode spectrum in a consistent way. Period spacings, rotational splittings, mode widths, and mode heights, all depend on the mode inertia so that all are related to the parameter  $\zeta$ . We could derive interesting properties:

- The asymptotic fit of the mixed modes proves to be precise and unbiased. Its precision for the RGB stars is so high that the asymptotic expansion of gravity modes can be validated when buoyancy glitches are absent. This ensures the delivery of accurate asymptotic parameters  $\Delta\Pi_1$ ,  $q$ , and  $\varepsilon_g$ . We found only one RGB star with such buoyancy glitches; on the contrary, buoyancy glitches are often present in red-clump stars.

- The period spacings and rotational splittings are better estimated with integrated values of the function  $\zeta$ . The use of these mean values  $\langle\zeta\rangle_n$  and  $\langle\zeta\rangle_m$  is useful for evolved RGB stars and is mandatory for stars with intricate splittings and spacings. Using the stretched period (Mosser et al. 2015) is in fact equivalent.

- The gravity asymptotic parameters  $\Delta\Pi_1$  and  $\varepsilon_g$  can now be accurately determined, with typical accuracy of respectively 0.06 s and 0.1 on the RGB, and 0.22 s and 0.08 in the red clump. This opens the way to a fruitful dialogue with theoretical developments (Takata 2006, 2016b,a) and modeling (e.g., Bossini et al. 2015; Cunha et al. 2015).

- We have made clear that observing mixed modes in evolved red giants requires an observation duration longer than  $\simeq 100$  days. However, gravity-dominated mixed modes are no longer observable when the stars are more evolved than  $\Delta\nu \simeq 6 \mu\text{Hz}$  on the RGB, or  $\Delta\nu \simeq 3 \mu\text{Hz}$  in the red clump. These thresholds are indicative values: the natural spread of the seismic parameters with respect to their mean values explain slight differences.

- We have demonstrated the non-alignment of the rotation axis of the stars belonging to the old open clusters NGC 6791 and NGC 6819. These results contradict previous findings by Corsaro et al. (2017) and illustrate how useful the asymptotic fit will be in the future when used to define priors to any Bayesian or other type of fit of mixed modes.

*Acknowledgements.* We thank the entire *Kepler* team, whose efforts made these results possible. BM warmly thanks Yvonne Elsworth, James Kuszlewicz and Masao Takata for their comments on the draft submitted for internal review on the website of the *Kepler* Asteroseismic Science Operations Center. We acknowledge financial support from the Programme National de Physique Stellaire (CNRS/INSU). BM acknowledges the support of the International Space Institute (ISSI) for the program AsteroSTEP (Asteroseismology of STEllar Populations)

## References

- Albareti, F. D., Allende Prieto, C., Almeida, A., et al. 2017, *ApJS*, 233, 25
- Appourchaux, T., Berthomieu, G., Michel, E., et al. 2006, in *ESA Special Publication, Vol. 1306, The CoRoT Mission Pre-Launch Status - Stellar Seismology and Planet Finding*, ed. M. Fridlund, A. Baglin, J. Lochard, & L. Conroy, 377
- Basu, S., Grundahl, F., Stello, D., et al. 2011, *ApJ*, 729, L10
- Baudin, F., Barban, C., Goupil, M. J., et al. 2012, *A&A*, 538, A73
- Beck, P. G., Bedding, T. R., Mosser, B., et al. 2011, *Science*, 332, 205
- Beck, P. G., Montalbán, J., Kallinger, T., et al. 2012, *Nature*, 481, 55
- Bedding, T. R., Mosser, B., Huber, D., et al. 2011, *Nature*, 471, 608
- Belkacem, K., Marques, J. P., Goupil, M. J., et al. 2015a, *A&A*, 579, A31
- Belkacem, K., Marques, J. P., Goupil, M. J., et al. 2015b, *A&A*, 579, A30
- Benomar, O., Bedding, T. R., Mosser, B., et al. 2013, *ApJ*, 767, 158
- Benomar, O., Belkacem, K., Bedding, T. R., et al. 2014, *ApJ*, 781, L29
- Bossini, D., Miglio, A., Salaris, M., et al. 2015, *MNRAS*, 453, 2290
- Bossini, D., Miglio, A., Salaris, M., et al. 2017, *MNRAS*, 469, 4718
- Buysschaert, B., Beck, P. G., Corsaro, E., et al. 2016, *A&A*, 588, A82
- Christensen-Dalsgaard, J. 2012, in *Astronomical Society of the Pacific Conference Series, Vol. 462, Progress in Solar/Stellar Physics with Helio- and Asteroseismology*, ed. H. Shibahashi, M. Takata, & A. E. Lynas-Gray, 503
- Corsaro, E., De Ridder, J., & García, R. A. 2015, *A&A*, 579, A83
- Corsaro, E., De Ridder, J., & García, R. A. 2018, *A&A*, 612, C2
- Corsaro, E., Lee, Y.-N., García, R. A., et al. 2017, *Nature Astronomy*, 1, 0064
- Cunha, M. S., Stello, D., Avelino, P. P., Christensen-Dalsgaard, J., & Townsend, R. H. D. 2015, *ApJ*, 805, 127
- Deheuvels, S., Ballot, J., Beck, P. G., et al. 2015, *A&A*, 580, A96
- Deheuvels, S., Doğan, G., Goupil, M. J., et al. 2014, *A&A*, 564, A27
- Deheuvels, S., Ouazzani, R. M., & Basu, S. 2017, *A&A*, 605, A75
- Di Mauro, M. P., Ventura, R., Cardini, D., et al. 2016, *ApJ*, 817, 65
- Dupret, M., Belkacem, K., Samadi, R., et al. 2009, *A&A*, 506, 57
- Elsworth, Y., Hekker, S., Basu, S., & Davies, G. R. 2017, *MNRAS*, 466, 3344
- García, R. A., Hekker, S., Stello, D., et al. 2011, *MNRAS*, 414, L6
- García, R. A., Pérez Hernández, F., Benomar, O., et al. 2014, *A&A*, 563, A84
- García Saravia Ortiz de Montellano, A., Hekker, S., & Themeßl, N. 2018, *MNRAS*, 476, 1470
- Gaulme, P., Appourchaux, T., & Boumier, P. 2009, *A&A*, 506, 7
- Gehan, C., Mosser, B., & Michel, E. 2016, *ArXiv e-prints*
- Gehan, C., Mosser, B., & Michel, E. 2017, in *European Physical Journal Web of Conferences, Vol. 160, European Physical Journal Web of Conferences, 04005*
- Gehan, C., Mosser, B., Michel, E., Samadi, R., & Kallinger, T. 2018, *ArXiv e-prints*
- Goupil, M. J., Mosser, B., Marques, J. P., et al. 2013, *A&A*, 549, A75
- Grosjean, M., Dupret, M.-A., Belkacem, K., et al. 2014, *A&A*, 572, A11
- Handberg, R., Brogaard, K., Miglio, A., et al. 2017, *MNRAS*, 472, 979
- Hekker, S. & Christensen-Dalsgaard, J. 2017, *A&A Rev.*, 25

- Hekker, S., Elsworth, Y., & Angelou, G. C. 2018, *A&A*, 610, A80
- Jenkins, J. M., Caldwell, D. A., Chandrasekaran, H., et al. 2010, *ApJ*, 713, L87
- Kallinger, T., Hekker, S., Mosser, B., et al. 2012, *A&A*, 541, A51
- Khan, S., Hall, O. J., Miglio, A., et al. 2018, *ApJ*, 859, 156
- Lagarde, N., Bossini, D., Miglio, A., Vrad, M., & Mosser, B. 2016, *MNRAS*, 457, L59
- Libbrecht, K. G. 1992, *ApJ*, 387, 712
- Miglio, A., Brogaard, K., Stello, D., et al. 2012, *MNRAS*, 419, 2077
- Miglio, A., Chiappini, C., Mosser, B., et al. 2017, *Astronomische Nachrichten*, 338, 644
- Miglio, A., Montalbán, J., Carrier, F., et al. 2010, *A&A*, 520, L6
- Montalbán, J., Miglio, A., Noels, A., et al. 2013, *ApJ*, 766, 118
- Mosser, B. & Appourchaux, T. 2009, *A&A*, 508, 877
- Mosser, B., Barban, C., Montalbán, J., et al. 2011a, *A&A*, 532, A86
- Mosser, B., Belkacem, K., Goupil, M., et al. 2011b, *A&A*, 525, L9
- Mosser, B., Belkacem, K., Pinçon, C., et al. 2017a, *A&A*, 598, A62
- Mosser, B., Benomar, O., Belkacem, K., et al. 2014, *A&A*, 572, L5
- Mosser, B., Dziembowski, W. A., Belkacem, K., et al. 2013, *A&A*, 559, A137
- Mosser, B., Elsworth, Y., Hekker, S., et al. 2012a, *A&A*, 537, A30
- Mosser, B., Goupil, M. J., Belkacem, K., et al. 2012b, *A&A*, 540, A143
- Mosser, B., Goupil, M. J., Belkacem, K., et al. 2012c, *A&A*, 548, A10
- Mosser, B., Pinçon, C., Belkacem, K., Takata, M., & Vrad, M. 2017b, *A&A*, 600, A1
- Mosser, B., Vrad, M., Belkacem, K., Deheuvels, S., & Goupil, M. J. 2015, *A&A*, 584, A50
- Ouazzani, R.-M., Goupil, M. J., Dupret, M.-A., & Marques, J. P. 2013, *A&A*, 554, A80
- Provost, J. & Berthomieu, G. 1986, *A&A*, 165, 218
- Shibahashi, H. 1979, *PASJ*, 31, 87
- Stello, D., Compton, D. L., Bedding, T. R., et al. 2014, *ApJ*, 788, L10
- Stello, D., Meibom, S., Gilliland, R. L., et al. 2011, *ApJ*, 739, 13
- Stello, D., Zinn, J., Elsworth, Y., et al. 2017, *ApJ*, 835, 83
- Takata, M. 2006, *PASJ*, 58, 893
- Takata, M. 2016a, *PASJ*, 68, 109
- Takata, M. 2016b, *PASJ*, 68, 91
- Tassoul, M. 1980, *ApJS*, 43, 469
- Triana, S. A., Corsaro, E., De Ridder, J., et al. 2017, *A&A*, 602, A62
- Unno, W., Osaki, Y., Ando, H., Saio, H., & Shibahashi, H. 1989, *Nonradial oscillations of stars*, ed. Unno, W., Osaki, Y., Ando, H., Saio, H., & Shibahashi, H.
- Vrad, M., Kallinger, T., Mosser, B., et al. 2018, *ArXiv e-prints*
- Vrad, M., Mosser, B., Barban, C., et al. 2015, *A&A*, 579, A84
- Vrad, M., Mosser, B., & Samadi, R. 2016, *A&A*, 588, A87

pure numerical approach is the next step for delivering duly identified mixed modes.

The échelle diagrams of the stars mentioned in the main text are also presented:

- KIC 10272858 lies on the low part of the RGB (Fig. A.1);
- KIC 11353313 is on the RGB (Fig. A.2);
- KIC 3955033 is a RGB star with a rapid core rotation (Fig. A.3); its frequencies are given in Table A.2;
- KIC 2443903 is more evolved on the RGB, at the limit of detection of mixed modes (Fig. A.4);
- KIC 1723700 is in the red clump star (Fig. A.5);
- and KIC 1725190 is a secondary red clump star (Fig. A.6).

## Appendix A: Seismic parameters

We used KIC 6144777 as a case study (Fig. 2). Table A.1 provides the fit of its radial dipole mixed modes. Our results are in agreement with those published by Corsaro et al. (2015) and derive a similar number of modes (about 100), but also show differences:

- The determination of the frequencies in Corsaro et al. (2015) can be as precise as 0.3 nHz. This precision of about  $\delta f_{\text{res}}/30$  was corrected into about  $\delta f_{\text{res}}/10$  in their corrigendum (Corsaro et al. 2018), which remains surprisingly good; the frequencies we obtain are given with a precision that is at best about half the frequency resolution ( $\simeq 4$  nHz).
- Their mode widths are quite different and, most often, larger than ours;
- Heights also differ, which can come from a different treatment of the time series.

A large agreement is also met with the results obtained by García Saravia Ortiz de Montellano et al. (2018) with a peak detection algorithm that works in a fully blind manner, if we relax their uncertainties that can be as low as  $\delta f_{\text{res}}/20$ .

The potential of the comparison between methods based on different principles is very high: coupling the physics of the asymptotic expansion and the power of a



**Table A.1.** Oscillation pattern of the RGB star KIC 6144777

$n_p$	$n$	$m$	$\zeta$	$\nu_{\text{as}}$ ( $\mu\text{Hz}$ )	$\nu$ ( $\mu\text{Hz}$ )	$x$	$\Gamma_{\text{as}}$ ( $\mu\text{Hz}$ )	$\Gamma$ ( $\mu\text{Hz}$ )	$H$ ( $\text{ppm}^2\mu\text{Hz}^{-1}$ )	$R$
Radial modes										
8				101.916	101.916 $\pm$ 0.014	0.040		0.120 $\pm$ 0.023	1390 $\pm$ 316	24.1
9				112.612	112.612 $\pm$ 0.011	0.010		0.106 $\pm$ 0.016	3314 $\pm$ 497	85.2
10				123.726	123.622 $\pm$ 0.006	0.008		0.054 $\pm$ 0.007	23358 $\pm$ 3059	338.5
11				134.574	134.534 $\pm$ 0.008	-0.003		0.087 $\pm$ 0.012	10451 $\pm$ 1305	195.7
12				145.842	145.585 $\pm$ 0.017	-0.002		0.244 $\pm$ 0.057	1491 $\pm$ 441	26.6
13				156.846	156.846 $\pm$ 0.042	0.019		0.258 $\pm$ 0.074	317 $\pm$ 121	10.7
Dipole mixed modes										
8	-112	1	0.9522	105.827	105.836 $\pm$ 0.007	0.396	0.009	0.007 $\pm$ 0.004	1185 $\pm$ 281	10.1
8	-111	1	0.8506	106.633	106.648 $\pm$ 0.007	0.469	0.027	0.011 $\pm$ 0.004	2124 $\pm$ 440	26.0
8	-110	-1	0.7311	106.957	106.985 $\pm$ 0.014	0.500	0.048	0.068 $\pm$ 0.017	454 $\pm$ 149	14.5
8	-110	0	0.6467	107.134	107.137 $\pm$ 0.010	0.514	0.064	0.042 $\pm$ 0.009	658 $\pm$ 145	13.9
8	-110	1	0.5989	107.278	107.322 $\pm$ 0.008	0.530	0.072	0.040 $\pm$ 0.007	1497 $\pm$ 250	30.6
8	-109	-1	0.6428	107.551	107.604 $\pm$ 0.009	0.556	0.064	0.055 $\pm$ 0.011	1272 $\pm$ 292	17.8
8	-109	0	0.7161	107.706	107.730 $\pm$ 0.010	0.567	0.051	0.036 $\pm$ 0.008	630 $\pm$ 157	11.2
8	-109	1	0.7983	107.899	107.909 $\pm$ 0.007	0.584	0.036	0.018 $\pm$ 0.005	1646 $\pm$ 323	18.0
8	-108	-1	0.8911	108.264	108.263 $\pm$ 0.010	0.616	0.020	0.016 $\pm$ 0.005	770 $\pm$ 254	12.2
8	-108	0	0.9206	108.482	108.484 $\pm$ 0.006	0.636	0.014	0.007 $\pm$ 0.004	1554 $\pm$ 335	14.0
8	-108	1	0.9406	108.710	108.700 $\pm$ 0.011	0.655	0.011	0.014 $\pm$ 0.005	505 $\pm$ 186	8.8
8	-107	-1	0.9617	109.140	109.138 $\pm$ 0.007	0.695	0.007	0.006 $\pm$ 0.004	1303 $\pm$ 313	11.9
8	-107	0	0.9683	109.373	109.375 $\pm$ 0.008	0.716	0.006	0.005 $\pm$ 0.004	783 $\pm$ 323	7.2
8	-106	0	0.9822	110.304	110.274 $\pm$ 0.008	0.798	0.003	0.006 $\pm$ 0.004	803 $\pm$ 175	8.4
8	-104	0	0.9889	112.235	112.235 $\pm$ 0.007	-0.024	0.002	0.005 $\pm$ 0.004	959 $\pm$ 335	9.3
9	-103	-1	0.9889	112.989	113.018 $\pm$ 0.012	0.047	0.002	0.006 $\pm$ 0.004	739 $\pm$ 269	8.1
9	-103	0	0.9889	113.228	113.226 $\pm$ 0.006	0.065	0.002	0.005 $\pm$ 0.004	1736 $\pm$ 480	17.3
9	-102	-1	0.9872	113.999	113.996 $\pm$ 0.007	0.135	0.002	0.006 $\pm$ 0.004	789 $\pm$ 174	8.2
9	-102	1	0.9856	114.477	114.478 $\pm$ 0.007	0.179	0.003	0.005 $\pm$ 0.004	919 $\pm$ 297	9.4
9	-101	0	0.9800	115.262	115.254 $\pm$ 0.008	0.249	0.004	0.005 $\pm$ 0.004	701 $\pm$ 221	7.3
9	-100	-1	0.9672	116.058	116.058 $\pm$ 0.006	0.322	0.006	0.006 $\pm$ 0.004	1721 $\pm$ 254	19.0
9	-100	0	0.9600	116.292	116.285 $\pm$ 0.007	0.343	0.007	0.006 $\pm$ 0.004	1150 $\pm$ 273	12.1
9	-100	1	0.9506	116.523	116.525 $\pm$ 0.006	0.364	0.009	0.006 $\pm$ 0.004	2571 $\pm$ 532	27.2
9	-99	-1	0.9056	117.072	117.076 $\pm$ 0.009	0.414	0.017	0.022 $\pm$ 0.006	459 $\pm$ 134	12.7
9	-99	0	0.8694	117.291	117.318 $\pm$ 0.025	0.436	0.023	0.040 $\pm$ 0.013	77 $\pm$ 34	7.2
9	-99	1	0.8189	117.489	117.520 $\pm$ 0.006	0.455	0.033	0.011 $\pm$ 0.004	4320 $\pm$ 641	54.2
9	-98	-1	0.6256	117.926	117.973 $\pm$ 0.007	0.496	0.067	0.043 $\pm$ 0.007	2105 $\pm$ 327	32.6
9	-98	0	0.5622	118.077	118.138 $\pm$ 0.009	0.511	0.079	0.033 $\pm$ 0.007	5534 $\pm$ 1222	91.7
9	-98	1	0.5461	118.211	118.282 $\pm$ 0.009	0.524	0.082	0.034 $\pm$ 0.007	3206 $\pm$ 652	69.8
9	-97	-1	0.6989	118.597	118.638 $\pm$ 0.008	0.556	0.054	0.034 $\pm$ 0.007	3294 $\pm$ 723	142.5
9	-97	0	0.7744	118.766	118.815 $\pm$ 0.007	0.572	0.041	0.013 $\pm$ 0.004	3831 $\pm$ 566	66.2
9	-97	1	0.8394	118.969	118.994 $\pm$ 0.006	0.588	0.029	0.010 $\pm$ 0.004	10109 $\pm$ 1478	154.7
9	-96	-1	0.9267	119.532	119.539 $\pm$ 0.008	0.638	0.013	0.017 $\pm$ 0.005	1339 $\pm$ 307	23.5
9	-96	0	0.9428	119.758	119.758 $\pm$ 0.006	0.658	0.010	0.008 $\pm$ 0.004	4038 $\pm$ 588	46.3
9	-96	1	0.9539	119.989	119.991 $\pm$ 0.007	0.679	0.008	0.008 $\pm$ 0.004	2271 $\pm$ 444	25.7
9	-95	-1	0.9717	120.623	120.617 $\pm$ 0.006	0.735	0.005	0.006 $\pm$ 0.004	3853 $\pm$ 586	44.1
9	-95	1	0.9778	121.096	121.088 $\pm$ 0.006	0.778	0.004	0.006 $\pm$ 0.004	6667 $\pm$ 971	77.7
9	-94	-1	0.9828	121.763	121.749 $\pm$ 0.006	-0.162	0.003	0.006 $\pm$ 0.004	5234 $\pm$ 769	61.2
9	-93	-1	0.9867	122.933	122.925 $\pm$ 0.010	-0.055	0.002	0.007 $\pm$ 0.004	2021 $\pm$ 647	27.2
10	-92	0	0.9861	124.367	124.355 $\pm$ 0.006	0.074	0.002	0.006 $\pm$ 0.004	1007 $\pm$ 169	13.4
10	-91	-1	0.9833	125.344	125.329 $\pm$ 0.007	0.162	0.003	0.005 $\pm$ 0.004	2714 $\pm$ 740	33.8
10	-91	0	0.9817	125.582	125.568 $\pm$ 0.006	0.184	0.003	0.005 $\pm$ 0.004	1574 $\pm$ 381	19.7
10	-91	1	0.9800	125.819	125.796 $\pm$ 0.006	0.205	0.004	0.006 $\pm$ 0.004	5347 $\pm$ 831	67.2
10	-90	-1	0.9706	126.575	126.561 $\pm$ 0.007	0.274	0.005	0.006 $\pm$ 0.004	1987 $\pm$ 407	25.3
10	-90	0	0.9661	126.810	126.799 $\pm$ 0.008	0.296	0.006	0.009 $\pm$ 0.004	2797 $\pm$ 714	35.8
10	-90	1	0.9594	127.042	127.032 $\pm$ 0.006	0.317	0.007	0.006 $\pm$ 0.004	5283 $\pm$ 1186	67.9
10	-89	-1	0.9167	127.792	127.789 $\pm$ 0.006	0.385	0.015	0.010 $\pm$ 0.004	2454 $\pm$ 424	31.9
10	-89	0	0.8900	128.014	128.018 $\pm$ 0.007	0.406	0.020	0.007 $\pm$ 0.004	1441 $\pm$ 297	18.8
10	-89	1	0.8528	128.220	128.231 $\pm$ 0.007	0.425	0.026	0.009 $\pm$ 0.004	6599 $\pm$ 1274	92.5
10	-88	-1	0.6144	128.822	128.875 $\pm$ 0.008	0.484	0.069	0.021 $\pm$ 0.005	6832 $\pm$ 1038	132.3
10	-88	0	0.5406	128.970	129.032 $\pm$ 0.008	0.498	0.083	0.043 $\pm$ 0.007	3925 $\pm$ 617	91.8
10	-88	1	0.5044	129.095	129.168 $\pm$ 0.009	0.510	0.089	0.034 $\pm$ 0.007	5624 $\pm$ 1181	130.5
10	-87	-1	0.6672	129.569	129.608 $\pm$ 0.009	0.550	0.060	0.049 $\pm$ 0.010	3066 $\pm$ 755	157.3
10	-87	0	0.7439	129.731	129.772 $\pm$ 0.007	0.565	0.046	0.014 $\pm$ 0.004	12352 $\pm$ 1855	257.9
10	-87	1	0.8133	129.927	129.955 $\pm$ 0.006	0.582	0.034	0.011 $\pm$ 0.004	16357 $\pm$ 2408	226.5
10	-86	-1	0.9294	130.677	130.670 $\pm$ 0.006	0.647	0.013	0.007 $\pm$ 0.004	4084 $\pm$ 855	55.9
10	-86	0	0.9433	130.903	130.896 $\pm$ 0.006	0.667	0.010	0.007 $\pm$ 0.004	7019 $\pm$ 1024	96.4
10	-86	1	0.9533	131.134	131.122 $\pm$ 0.006	0.688	0.008	0.006 $\pm$ 0.004	10575 $\pm$ 2196	145.8
10	-85	-1	0.9728	131.986	131.962 $\pm$ 0.009	0.764	0.005	0.009 $\pm$ 0.004	1419 $\pm$ 431	19.8
10	-85	0	0.9756	132.221	132.196 $\pm$ 0.009	0.785	0.004	0.006 $\pm$ 0.004	530 $\pm$ 151	7.4
10	-84	0	0.9833	133.590	133.573 $\pm$ 0.006	-0.090	0.003	0.006 $\pm$ 0.004	3228 $\pm$ 566	46.4
11	-83	0	0.9844	134.993	134.973 $\pm$ 0.006	0.037	0.003	0.006 $\pm$ 0.004	4520 $\pm$ 719	66.5
11	-82	-1	0.9806	136.185	136.161 $\pm$ 0.006	0.144	0.004	0.006 $\pm$ 0.004	1267 $\pm$ 184	20.0
11	-81	-1	0.9639	137.632	137.609 $\pm$ 0.006	0.275	0.007	0.006 $\pm$ 0.004	1148 $\pm$ 170	18.7
11	-81	0	0.9578	137.866	137.837 $\pm$ 0.007	0.296	0.008	0.006 $\pm$ 0.004	900 $\pm$ 151	13.9
11	-81	1	0.9494	138.096	138.075 $\pm$ 0.006	0.318	0.009	0.011 $\pm$ 0.004	2426 $\pm$ 366	39.1

Table A.1. continued.

$n_p$	$n$	$m$	$\zeta$	$\nu_{\text{as}}$ ( $\mu\text{Hz}$ )	$\nu$ ( $\mu\text{Hz}$ )	$x$	$\Gamma_{\text{as}}$ ( $\mu\text{Hz}$ )	$\Gamma$ ( $\mu\text{Hz}$ )	$H$ ( $\text{ppm}^2\mu\text{Hz}^{-1}$ )	$R$
11	-80	-1	0.8644	139.037	139.015 $\pm$ 0.007	0.403	0.024	0.012 $\pm$ 0.004	2323 $\pm$ 388	36.5
11	-80	0	0.8183	139.247	139.230 $\pm$ 0.006	0.422	0.033	0.020 $\pm$ 0.005	2879 $\pm$ 427	50.3
11	-80	1	0.7594	139.431	139.438 $\pm$ 0.007	0.441	0.043	0.029 $\pm$ 0.006	942 $\pm$ 147	18.2
11	-79	-1	0.4672	140.063	140.116 $\pm$ 0.009	0.503	0.096	0.078 $\pm$ 0.015	2479 $\pm$ 552	102.8
11	-79	0	0.4628	140.175	140.185 $\pm$ 0.012	0.509	0.097	0.128 $\pm$ 0.031	1534 $\pm$ 491	74.4
11	-79	1	0.4939	140.295	140.352 $\pm$ 0.009	0.524	0.091	0.071 $\pm$ 0.012	1831 $\pm$ 330	49.4
11	-78	-1	0.8100	140.998	141.019 $\pm$ 0.006	0.585	0.034	0.013 $\pm$ 0.004	3675 $\pm$ 536	61.6
11	-78	0	0.8550	141.194	141.202 $\pm$ 0.006	0.601	0.026	0.009 $\pm$ 0.004	3583 $\pm$ 541	58.3
11	-78	1	0.8894	141.409	141.419 $\pm$ 0.009	0.621	0.020	0.027 $\pm$ 0.007	1200 $\pm$ 332	44.1
11	-77	-1	0.9561	142.436	142.432 $\pm$ 0.006	0.713	0.008	0.007 $\pm$ 0.004	1831 $\pm$ 358	30.4
11	-77	0	0.9617	142.668	142.663 $\pm$ 0.006	0.734	0.007	0.006 $\pm$ 0.004	1912 $\pm$ 278	33.3
11	-77	1	0.9667	142.902	142.895 $\pm$ 0.009	0.755	0.006	0.009 $\pm$ 0.004	434 $\pm$ 133	7.3
12	-74	-1	0.9778	147.312	147.297 $\pm$ 0.007	0.154	0.004	0.005 $\pm$ 0.004	528 $\pm$ 146	9.4
12	-74	0	0.9761	147.549	147.551 $\pm$ 0.007	0.177	0.004	0.006 $\pm$ 0.004	557 $\pm$ 102	11.1
12	-74	1	0.9739	147.785	147.778 $\pm$ 0.006	0.197	0.005	0.006 $\pm$ 0.004	665 $\pm$ 120	12.0
12	-73	-1	0.9511	148.996	148.980 $\pm$ 0.009	0.306	0.009	0.010 $\pm$ 0.004	747 $\pm$ 193	18.1
12	-73	0	0.9422	149.226	149.215 $\pm$ 0.007	0.327	0.010	0.009 $\pm$ 0.004	756 $\pm$ 160	13.9
12	-73	1	0.9306	149.452	149.441 $\pm$ 0.006	0.348	0.013	0.011 $\pm$ 0.004	726 $\pm$ 122	14.3
12	-72	-1	0.7456	150.556	150.584 $\pm$ 0.008	0.452	0.046	0.041 $\pm$ 0.008	545 $\pm$ 112	18.2
12	-72	0	0.6672	150.737	150.764 $\pm$ 0.011	0.468	0.060	0.051 $\pm$ 0.011	298 $\pm$ 79	19.8
12	-72	1	0.5911	150.880	150.951 $\pm$ 0.011	0.485	0.074	0.060 $\pm$ 0.012	444 $\pm$ 99	23.6
12	-71	-1	0.4722	151.509	151.598 $\pm$ 0.010	0.543	0.095	0.067 $\pm$ 0.012	650 $\pm$ 126	27.4
12	-71	0	0.5300	151.624	151.720 $\pm$ 0.009	0.554	0.085	0.026 $\pm$ 0.006	1788 $\pm$ 329	66.9
12	-71	1	0.6122	151.772	151.861 $\pm$ 0.012	0.567	0.070	0.077 $\pm$ 0.018	380 $\pm$ 113	20.2
12	-70	1	0.9339	153.268	153.289 $\pm$ 0.007	0.697	0.012	0.007 $\pm$ 0.004	572 $\pm$ 100	12.3
12	-69	0	0.9717	154.828	154.849 $\pm$ 0.007	-0.162	0.005	0.005 $\pm$ 0.004	587 $\pm$ 160	11.7
12	-69	1	0.9733	155.064	155.083 $\pm$ 0.007	-0.141	0.005	0.006 $\pm$ 0.004	546 $\pm$ 97	11.8

$\zeta$  is derived from the best asymptotic fit;  $\nu_{\text{as}}$  are the asymptotic frequencies, whereas  $\nu$  correspond to the observed values;  $x = \nu/\Delta\nu - (n_p - \varepsilon_p)$  is the reduced frequency;  $\Gamma_{\text{as}}$  are the asymptotic mode widths, whereas  $\Gamma$  correspond to the observed values;  $H$  are the observed heights, and  $R$  is the height-to-background ratio.

## Appendix B: Stars in open clusters

All stars studied by Corsaro et al. (2017) were investigated. The fitting process is challenging, due to the dim magnitudes of such dim stars in open clusters. However, the combination of all pressure radial orders near  $\nu_{\max}$  provides in most cases an unambiguous fit, and at least a few mixed-mode radial orders provide clear splittings.

- Figure B.1 provides the asymptotic fit of KIC 5024476, member of the open cluster NGC 6819 observed by *Kepler*. We note that  $m = \pm 1$  modes are clearly identified and derive a stellar inclination  $i = 79 \pm 11^\circ$  for this star. This result is in disagreement with Corsaro et al. (2017) who found an inclination  $i = 20 \pm 7^\circ$ .

- Similar conclusions are reached for KIC 2437976 (Fig. B.2), member of the open cluster NGC 6791. Corsaro et al. (2017) found an inclination  $i = 0 \pm 10^\circ$ , despite the fact  $|m| = 1$  modes are clearly identified and indicate  $i = 76 \pm 14^\circ$ .

These stars are representative of the whole data set treated by Corsaro et al. (2017): the inability of the fitting process to identify thin short-lived mixed modes translates into the identification of a single broad  $m = 0$  peak. In such cases, stellar inclinations derived from the Bayesian fits are necessarily underestimated and biased toward low values.

**Table A.2.** Oscillation pattern of the RGB star KIC 3955033

$n_p$	$n$	$m$	$\zeta$	$\nu_{\text{as}}$ ( $\mu\text{Hz}$ )	$\nu$ ( $\mu\text{Hz}$ )	$x$	$\Gamma_{\text{as}}$ ( $\mu\text{Hz}$ )	$\Gamma$ ( $\mu\text{Hz}$ )	$H$ ( $\text{ppm}^2 \mu\text{Hz}^{-1}$ )	$R$
Radial modes										
8				84.745	$84.745 \pm 0.077$	0.033		$0.198 \pm 0.089$	$1015 \pm 656$	16.2
9				93.958	$93.762 \pm 0.012$	0.010		$0.094 \pm 0.017$	$3985 \pm 872$	27.3
10				102.911	$103.010 \pm 0.013$	0.012		$0.138 \pm 0.027$	$7641 \pm 1745$	30.2
11				112.215	$112.143 \pm 0.009$	0.002		$0.067 \pm 0.012$	$18117 \pm 3832$	114.7
12				121.869	$121.474 \pm 0.016$	0.013		$0.122 \pm 0.025$	$2495 \pm 637$	19.6
Dipole mixed modes										
8	-144	1	0.8744	88.882	$88.894 \pm 0.006$	0.483	0.019	$0.007 \pm 0.004$	$5748 \pm 1146$	15.9
8	-141	-1	0.8051	89.078	$89.075 \pm 0.009$	0.503	0.029	$0.020 \pm 0.005$	$2011 \pm 512$	7.1
8	-142	0	0.7444	89.214	$89.205 \pm 0.008$	0.517	0.038	$0.032 \pm 0.006$	$2964 \pm 565$	10.9
8	-143	1	0.6908	89.338	$89.338 \pm 0.010$	0.531	0.046	$0.041 \pm 0.009$	$2226 \pm 536$	15.9
8	-140	-1	0.6640	89.507	$89.496 \pm 0.007$	0.548	0.050	$0.035 \pm 0.006$	$6623 \pm 1063$	21.4
8	-141	0	0.6955	89.623	$89.602 \pm 0.011$	0.560	0.046	$0.036 \pm 0.008$	$1250 \pm 297$	10.1
8	-142	1	0.7483	89.743	$89.725 \pm 0.012$	0.573	0.038	$0.043 \pm 0.010$	$1315 \pm 389$	10.1
8	-139	-1	0.8432	89.969	$89.956 \pm 0.009$	0.598	0.023	$0.024 \pm 0.006$	$2118 \pm 541$	9.8
8	-141	1	0.9111	90.251	$90.238 \pm 0.009$	0.629	0.013	$0.006 \pm 0.004$	$2235 \pm 601$	7.4
9	-127	-1	0.9047	97.755	$97.779 \pm 0.011$	0.446	0.014	$0.023 \pm 0.007$	$1041 \pm 358$	9.9
9	-126	-1	0.6934	98.346	$98.392 \pm 0.007$	0.512	0.046	$0.014 \pm 0.004$	$36038 \pm 5534$	121.7
9	-127	0	0.6800	98.375	$98.395 \pm 0.007$	0.512	0.048	$0.024 \pm 0.005$	$21840 \pm 3803$	121.7
9	-128	1	0.6615	98.413	$98.395 \pm 0.007$	0.512	0.051	$0.027 \pm 0.005$	$19513 \pm 3160$	121.7
9	-125	-1	0.6969	98.825	$98.818 \pm 0.007$	0.558	0.045	$0.014 \pm 0.004$	$10668 \pm 1614$	47.6
9	-126	0	0.7049	98.843	$98.879 \pm 0.007$	0.565	0.044	$0.028 \pm 0.006$	$6104 \pm 971$	27.3
9	-127	1	0.7220	98.874	$98.883 \pm 0.007$	0.565	0.042	$0.031 \pm 0.006$	$5427 \pm 941$	27.3
9	-124	-1	0.9050	99.430	$99.435 \pm 0.006$	0.625	0.014	$0.006 \pm 0.004$	$9343 \pm 1572$	29.3
9	-126	1	0.9124	99.474	$99.470 \pm 0.006$	0.629	0.013	$0.012 \pm 0.004$	$7355 \pm 1118$	23.3
9	-125	1	0.9647	100.170	$100.166 \pm 0.007$	0.704	0.005	$0.006 \pm 0.004$	$2664 \pm 543$	9.3
10	-120	1	0.9883	103.940	$103.940 \pm 0.007$	0.113	0.002	$0.006 \pm 0.004$	$3119 \pm 574$	11.1
10	-118	-1	0.9880	104.023	$104.025 \pm 0.010$	0.122	0.002	$0.007 \pm 0.004$	$2677 \pm 836$	10.2
10	-118	0	0.9848	104.778	$104.780 \pm 0.011$	0.204	0.002	$0.007 \pm 0.004$	$2318 \pm 827$	9.3
10	-117	-1	0.9844	104.838	$104.842 \pm 0.009$	0.211	0.002	$0.006 \pm 0.004$	$4417 \pm 1446$	14.7
10	-116	-1	0.9748	105.657	$105.666 \pm 0.006$	0.300	0.004	$0.005 \pm 0.004$	$4718 \pm 1166$	15.8
10	-115	-1	0.9438	106.481	$106.502 \pm 0.022$	0.391	0.008	$0.019 \pm 0.011$	$1349 \pm 1022$	16.4
10	-116	1	0.8515	107.096	$107.070 \pm 0.008$	0.452	0.022	$0.008 \pm 0.004$	$1890 \pm 368$	10.1
10	-115	0	0.8294	107.167	$107.194 \pm 0.011$	0.466	0.026	$0.041 \pm 0.011$	$1090 \pm 354$	9.5
10	-114	-1	0.8023	107.238	$107.259 \pm 0.006$	0.473	0.030	$0.016 \pm 0.004$	$5430 \pm 799$	21.0
10	-115	1	0.5811	107.710	$107.706 \pm 0.007$	0.521	0.063	$0.019 \pm 0.005$	$22251 \pm 3274$	99.4
10	-114	0	0.5753	107.757	$107.776 \pm 0.011$	0.529	0.064	$0.082 \pm 0.021$	$3573 \pm 1204$	70.9
10	-113	-1	0.5782	107.819	$107.818 \pm 0.008$	0.533	0.063	$0.042 \pm 0.009$	$6466 \pm 1487$	71.0
10	-114	1	0.7802	108.260	$108.253 \pm 0.008$	0.580	0.033	$0.018 \pm 0.005$	$7228 \pm 1753$	32.4
10	-113	0	0.8149	108.344	$108.337 \pm 0.009$	0.589	0.028	$0.027 \pm 0.007$	$3135 \pm 809$	35.8
10	-112	-1	0.8468	108.441	$108.429 \pm 0.009$	0.599	0.023	$0.029 \pm 0.007$	$3843 \pm 1006$	25.7
10	-113	1	0.9383	109.023	$109.019 \pm 0.006$	0.663	0.009	$0.008 \pm 0.004$	$11460 \pm 1670$	41.2
10	-112	1	0.9728	109.876	$109.870 \pm 0.006$	0.756	0.004	$0.006 \pm 0.004$	$6439 \pm 938$	23.4
11	-104	-1	0.9239	115.807	$115.818 \pm 0.006$	0.400	0.011	$0.007 \pm 0.004$	$3908 \pm 613$	15.8
11	-105	1	0.8432	116.274	$116.279 \pm 0.006$	0.450	0.023	$0.009 \pm 0.004$	$6992 \pm 1054$	26.2
11	-104	0	0.7745	116.468	$116.470 \pm 0.009$	0.471	0.034	$0.033 \pm 0.008$	$1247 \pm 360$	18.8
11	-103	-1	0.6842	116.648	$116.670 \pm 0.007$	0.492	0.047	$0.028 \pm 0.006$	$2247 \pm 418$	28.7
11	-104	1	0.5371	116.961	$116.976 \pm 0.010$	0.525	0.069	$0.054 \pm 0.011$	$2255 \pm 530$	17.6
11	-103	0	0.5477	117.092	$117.077 \pm 0.015$	0.536	0.068	$0.082 \pm 0.021$	$1275 \pm 415$	19.0
11	-102	-1	0.6181	117.248	$117.211 \pm 0.010$	0.551	0.057	$0.028 \pm 0.007$	$1479 \pm 387$	11.9
11	-103	1	0.8015	117.612	$117.600 \pm 0.007$	0.593	0.030	$0.017 \pm 0.005$	$2633 \pm 464$	14.5
11	-101	-1	0.9071	118.072	$118.063 \pm 0.017$	0.643	0.014	$0.031 \pm 0.013$	$479 \pm 289$	10.9

 Radial modes and mixed modes identified in KIC 3955033 with a height-to-background ratio  $R$  larger than 7. Same caption as Table A.1

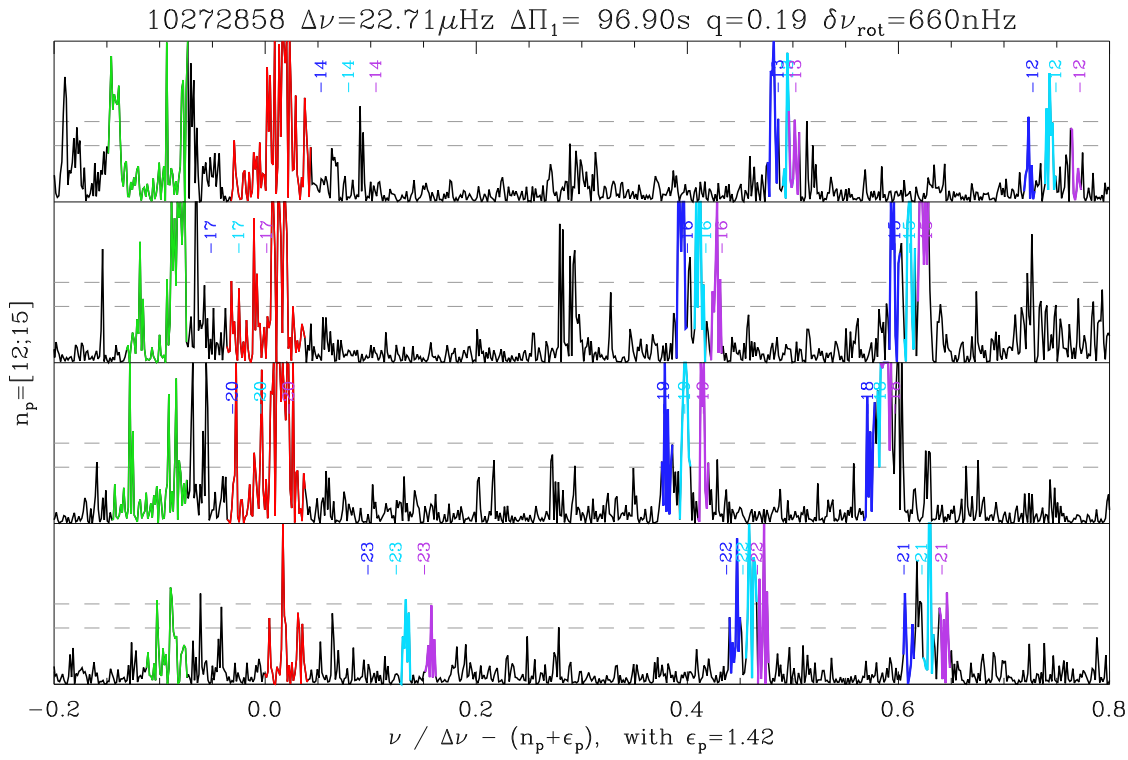


**Fig. A.1.** Fit of the oscillation pattern of the low RGB star KIC 10272858, at the limit of validity of the asymptotic pattern. Owing to the small radial orders, small shifts are seen between observed and asymptotic spectra. Same style as Fig. 2, but  $\ell = 3$  modes appear near the abscissa 0.28

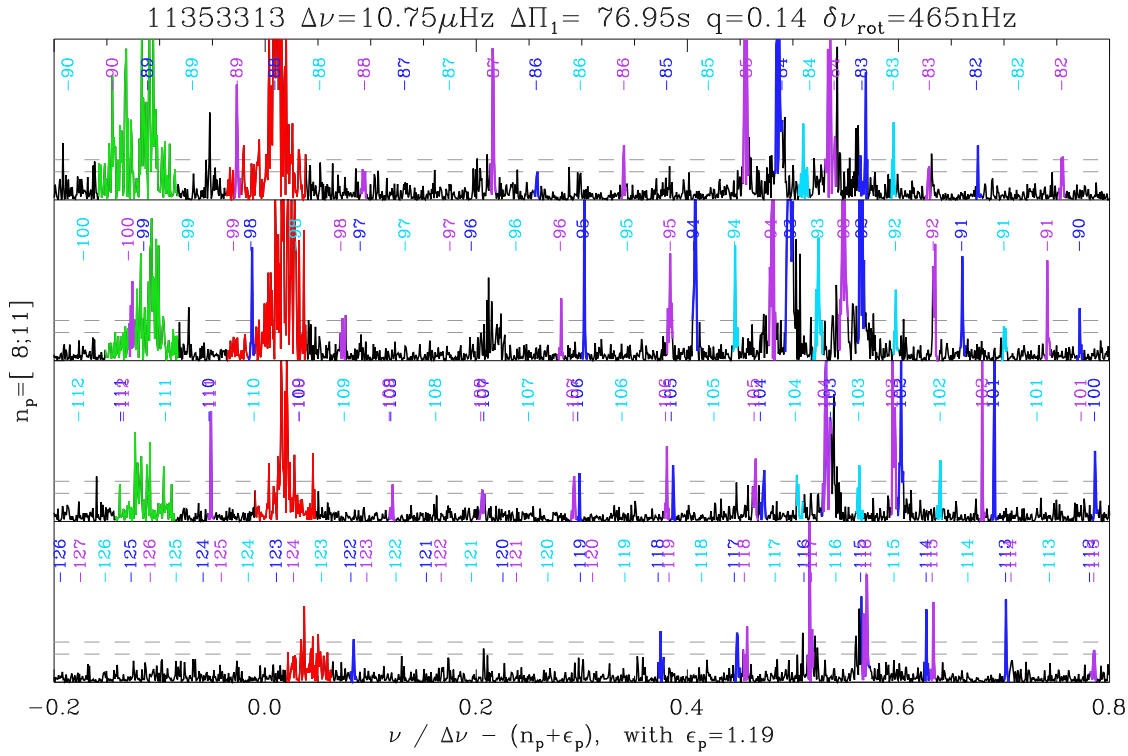


**Fig. A.2.** Fit of the oscillation pattern of the RGB star KIC 11353313. Same style as Fig. 2.

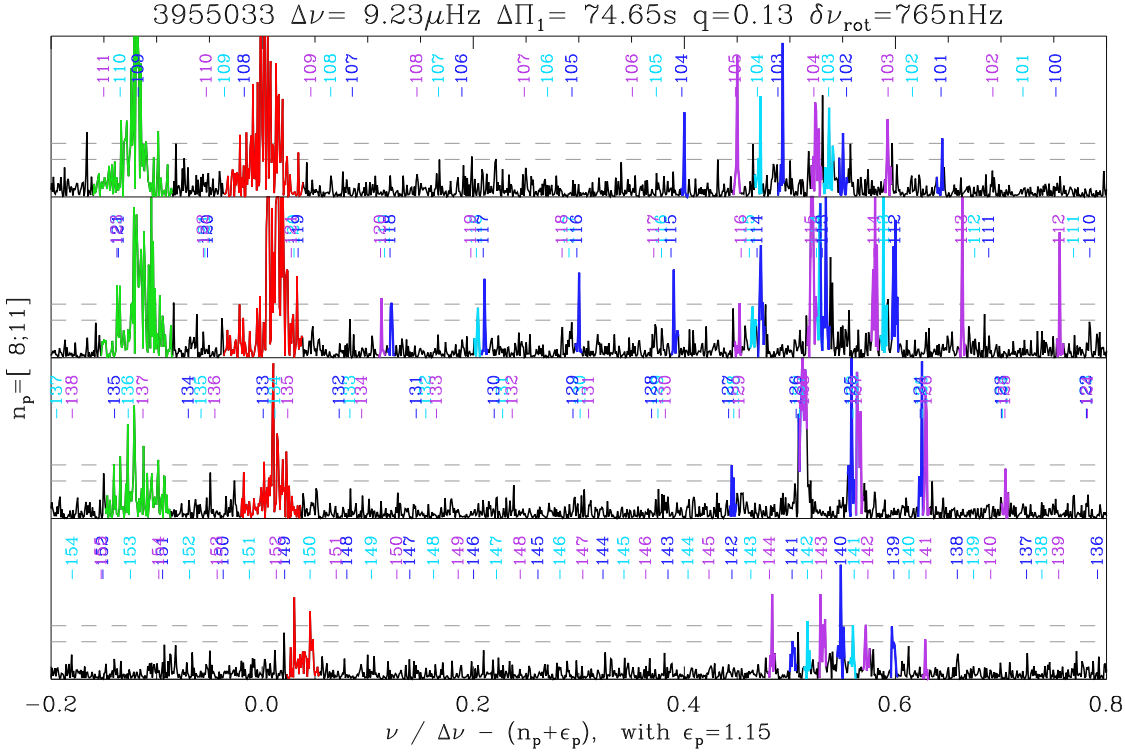


**Fig. A.3.** Fit of the oscillation pattern of the RGB star KIC 3955033. The overlap of mixed modes with different mixed-mode orders is the signature of the rapid core rotation. The second rotation crossing, where all components of the multiplets overlap (Gehan et al. 2017), occurs at the mixed-order  $n = -122$ . Same style as Fig. 2.

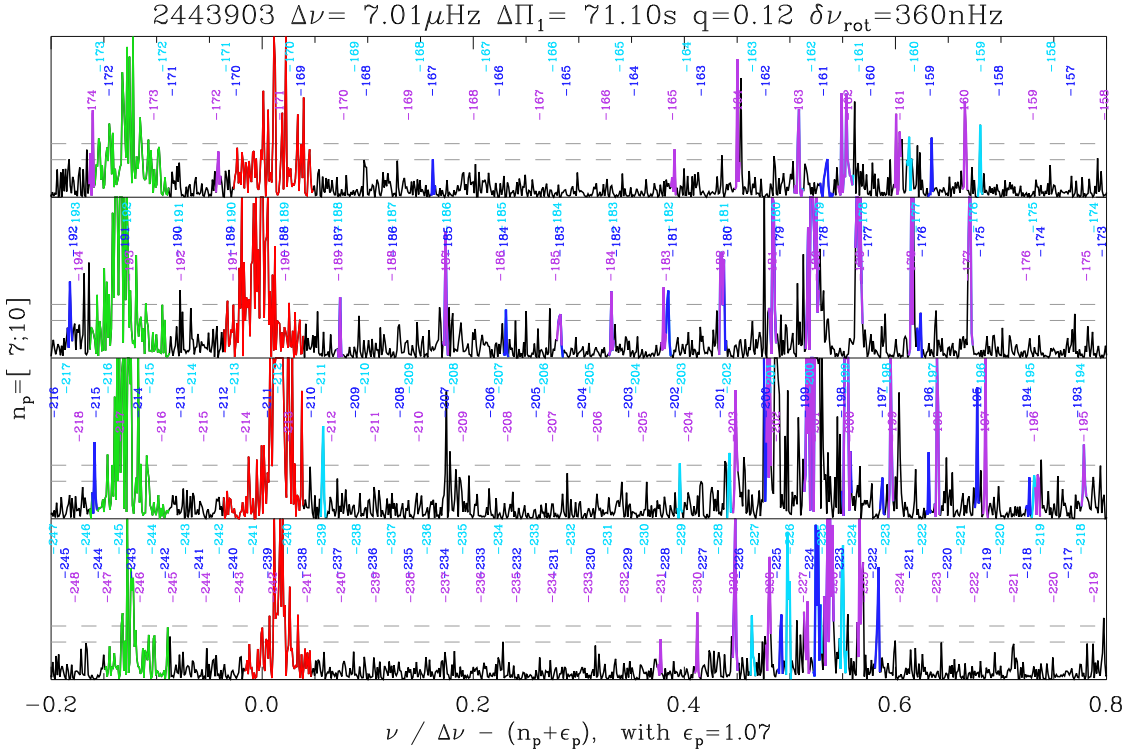


**Fig. A.4.** Fit of the oscillation pattern of the evolved RGB star KIC 2443903, near the limit of capability of identification, with a large crowding due to the high mode density. The second rotation crossing, where all  $m$  components apparently coincide, occurs at  $n = -189$  (with an abscissa  $\simeq 0.1$  and  $n_p = 9$ ); the third crossing, where  $|m| = 1$  components apparently coincide with  $m = 0$  inbetween, occurs at  $n = -233$  (with an abscissa  $\simeq 0.25$  and  $n_p = 7$ ). Same style as Fig. 2. Note that the modes with large heights at an abscissa  $\simeq 0.2$  are  $\ell = 3$  modes.

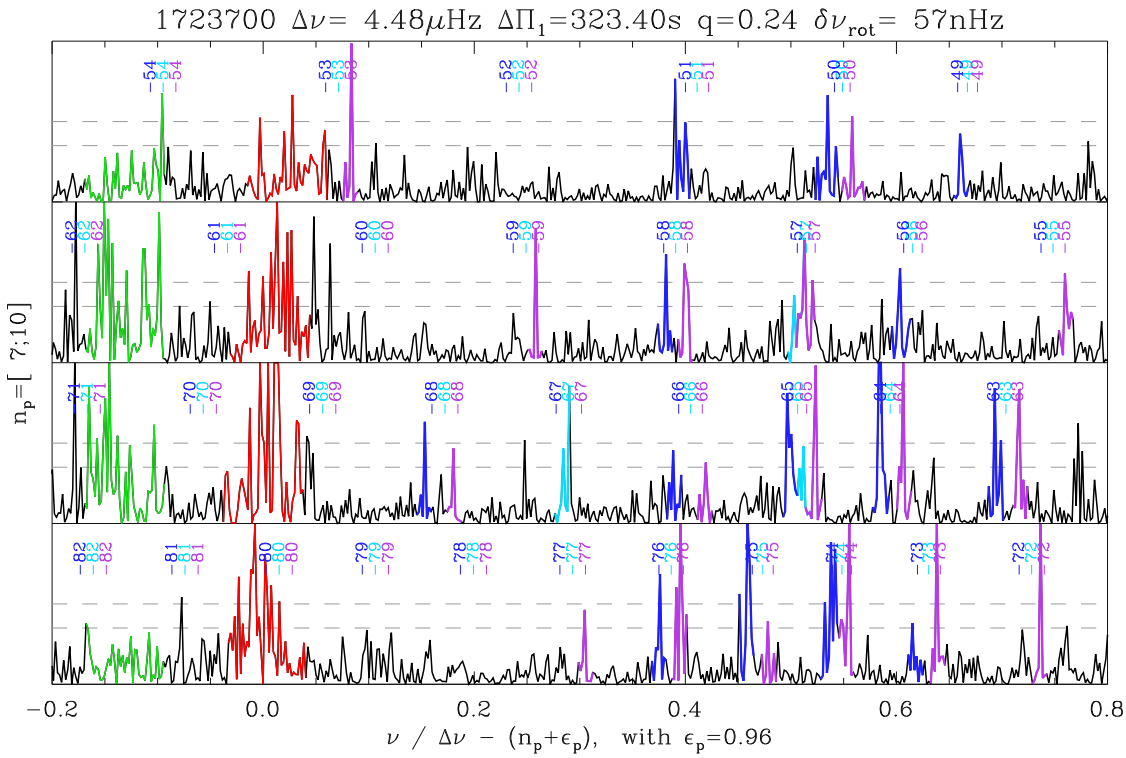


**Fig. A.5.** Fit of the oscillation pattern of the red-clump star KIC 1723700. Buoyancy glitches explain the small shifts between observed and asymptotic spectra but do not hamper the mode identification. Same style as Fig. 2.

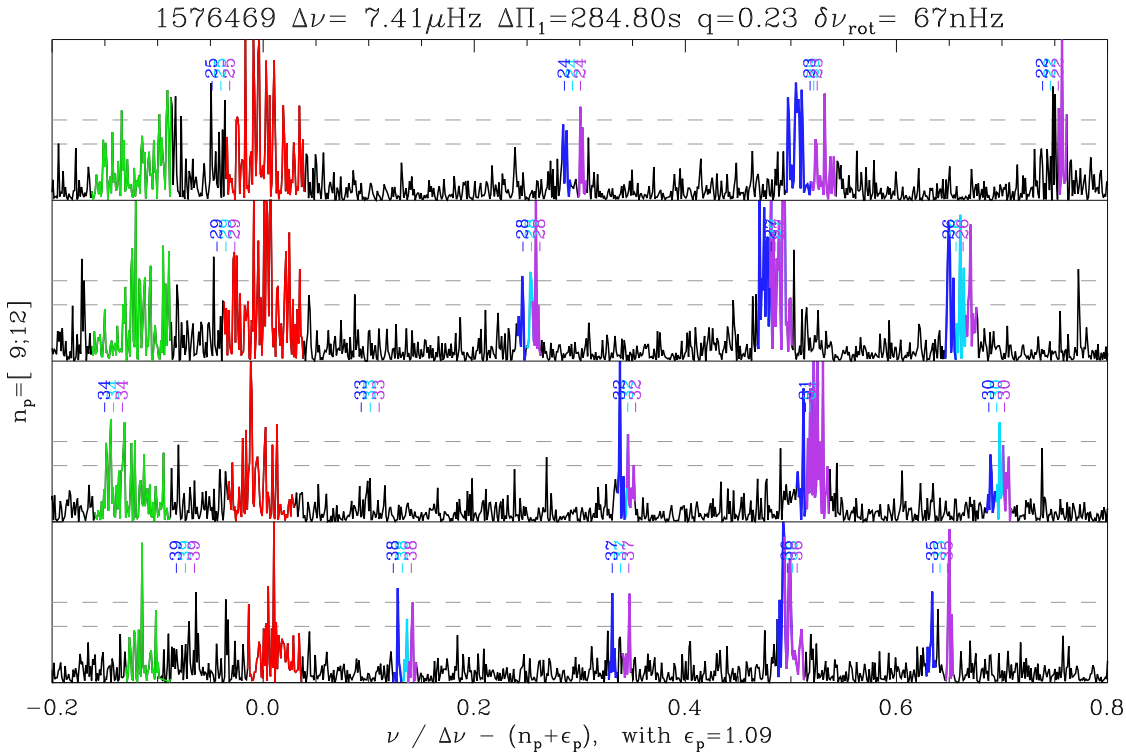


**Fig. A.6.** Fit of the oscillation pattern of the secondary-clump star KIC 1725190. Buoyancy glitches explain the small shifts between observed and asymptotic spectra but do not hamper the mode identification. Same style as Fig. 2.

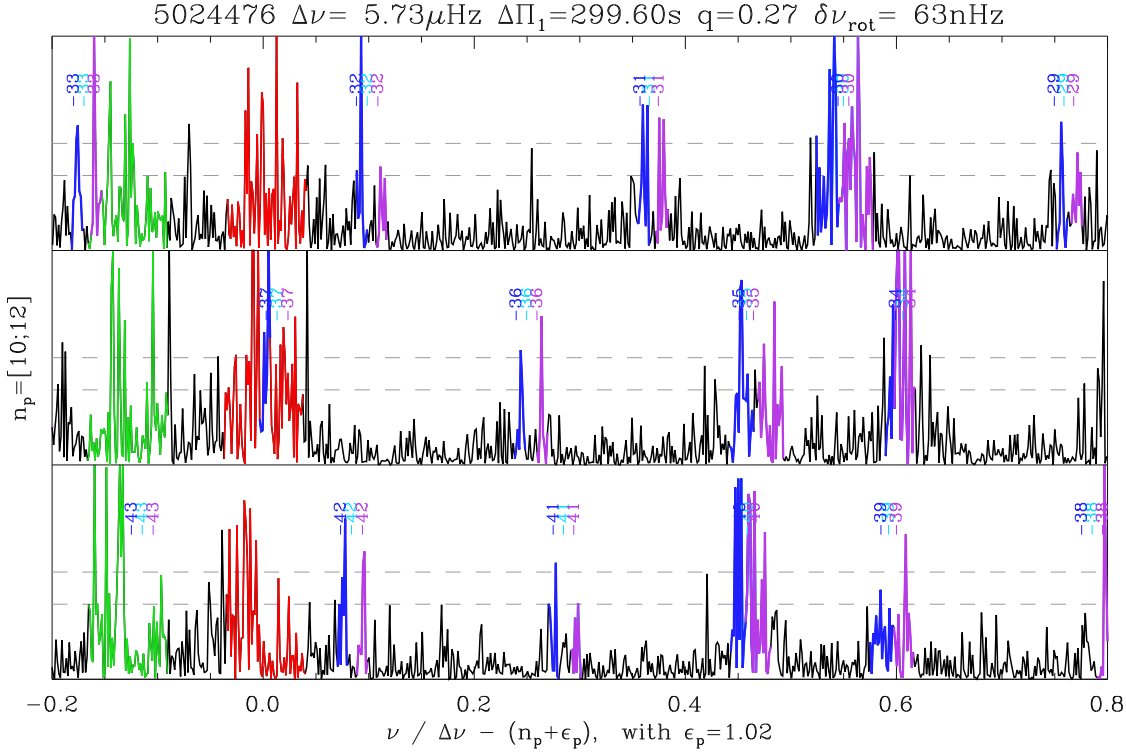


**Fig. B.1.** Fit of the oscillation pattern of the RGB star KIC 5024476, member of the open cluster NGC 6819. The dim magnitude of the cluster stars explains the low S/R. However, unambiguous doublets are identified all along the mixed-mode spectrum;  $m = 0$  modes are mostly absent and  $|m| = 1$  modes dominate the mixed-mode spectrum, so that a nearly pole-on inclination is not possible. Same style as Fig. 2.

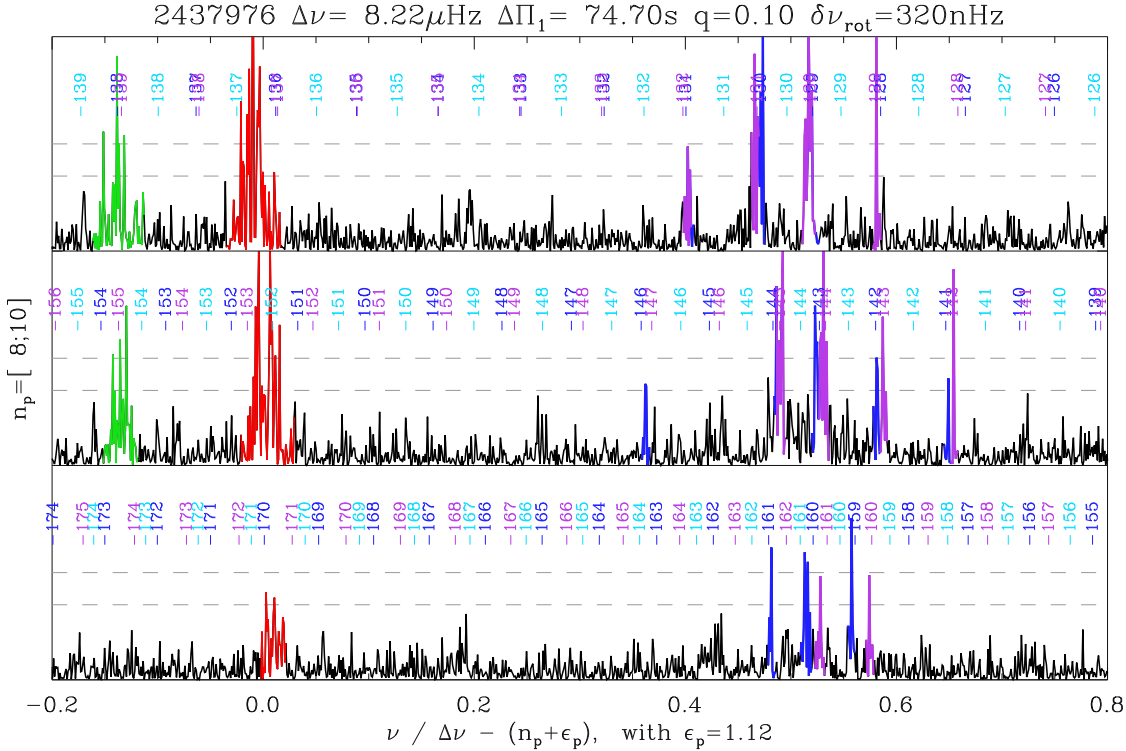


**Fig. B.2.** Fit of the oscillation pattern of the RGB star KIC 2437976, member of the open cluster NGC 6791. The dim magnitude of the cluster stars explains the low S/R. The identification at radial order 9, supported by the radial orders 8 and 10, is unambiguously conclusive:  $m = 0$  modes are mostly absent and  $|m| = 1$  modes dominate the mixed-mode spectrum, so that a pole-on inclination is not possible. Same style as Fig. 2.



**Table B.1.** Oscillation pattern of the red-clump star KIC 5024476 in NGC 6819

$n_p$	$n$	$m$	$\zeta$	$\nu_{\text{as}}$ ( $\mu\text{Hz}$ )	$\nu$ ( $\mu\text{Hz}$ )	$x$	$\Gamma_{\text{as}}$ ( $\mu\text{Hz}$ )	$\Gamma$ ( $\mu\text{Hz}$ )	$H$ ( $\text{ppm}^2 \mu\text{Hz}^{-1}$ )	$R$
Radial modes										
10				63.335	$63.096 \pm 0.174$	-0.058		$0.501 \pm 0.216$	$698 \pm 429$	9.9
11				69.039	$69.039 \pm 0.055$	-0.021		$0.350 \pm 0.102$	$1365 \pm 536$	9.7
12				74.941	$74.941 \pm 0.039$	0.009		$0.231 \pm 0.067$	$1158 \pm 452$	35.6
Dipole mixed modes										
10	-43	-1	0.9495	63.873	$63.870 \pm 0.009$	0.077	0.013	$0.019 \pm 0.006$	$1887 \pm 532$	16.0
10	-43	1	0.9481	63.979	$63.976 \pm 0.007$	0.095	0.013	$0.009 \pm 0.004$	$3002 \pm 632$	12.7
10	-42	-1	0.9006	65.035	$65.005 \pm 0.015$	0.275	0.025	$0.045 \pm 0.012$	$497 \pm 175$	11.6
10	-42	0	0.8955	65.086	$65.131 \pm 0.012$	0.297	0.026	$0.028 \pm 0.008$	$576 \pm 191$	7.6
10	-42	1	0.8903	65.136	$65.131 \pm 0.011$	0.297	0.027	$0.027 \pm 0.008$	$589 \pm 186$	7.6
10	-41	-1	0.6178	66.050	$66.050 \pm 0.013$	0.457	0.096	$0.095 \pm 0.020$	$1859 \pm 503$	20.0
10	-41	0	0.6011	66.085	$66.061 \pm 0.013$	0.459	0.100	$0.099 \pm 0.022$	$1959 \pm 563$	20.0
10	-41	1	0.5866	66.117	$66.083 \pm 0.014$	0.463	0.103	$0.106 \pm 0.025$	$1783 \pm 534$	18.7
10	-40	-1	0.6453	66.784	$66.788 \pm 0.017$	0.586	0.089	$0.085 \pm 0.020$	$800 \pm 240$	8.9
10	-40	1	0.6794	66.858	$66.897 \pm 0.020$	0.605	0.080	$0.097 \pm 0.023$	$632 \pm 197$	14.4
10	-39	1	0.9132	67.985	$68.003 \pm 0.007$	0.798	0.022	$0.009 \pm 0.004$	$4805 \pm 844$	23.5
11	-37	-1	0.9084	70.563	$70.562 \pm 0.007$	0.244	0.023	$0.009 \pm 0.004$	$2295 \pm 521$	11.4
11	-37	1	0.9003	70.665	$70.672 \pm 0.006$	0.264	0.025	$0.008 \pm 0.004$	$2474 \pm 398$	14.8
11	-36	-1	0.6140	71.776	$71.786 \pm 0.015$	0.458	0.097	$0.103 \pm 0.022$	$1228 \pm 333$	18.4
11	-36	1	0.5811	71.843	$71.884 \pm 0.019$	0.475	0.105	$0.127 \pm 0.030$	$854 \pm 264$	12.1
11	-35	-1	0.6100	72.588	$72.615 \pm 0.010$	0.603	0.097	$0.072 \pm 0.013$	$2715 \pm 560$	29.9
11	-35	1	0.6455	72.658	$72.625 \pm 0.011$	0.605	0.089	$0.078 \pm 0.015$	$2287 \pm 527$	29.9
11	-34	-1	0.9051	73.870	$73.881 \pm 0.007$	-0.176	0.024	$0.016 \pm 0.005$	$2320 \pm 417$	12.5
11	-34	1	0.9111	73.972	$73.977 \pm 0.007$	-0.160	0.022	$0.008 \pm 0.004$	$4124 \pm 750$	22.2
12	-33	-1	0.9314	75.420	$75.422 \pm 0.006$	0.093	0.017	$0.007 \pm 0.004$	$5610 \pm 987$	31.2
12	-33	1	0.9296	75.524	$75.530 \pm 0.008$	0.112	0.018	$0.008 \pm 0.004$	$1498 \pm 379$	8.3
12	-32	-1	0.8053	76.972	$76.954 \pm 0.008$	0.360	0.049	$0.024 \pm 0.006$	$1836 \pm 391$	14.5
12	-32	1	0.7828	77.061	$77.060 \pm 0.009$	0.379	0.054	$0.034 \pm 0.007$	$1103 \pm 222$	13.2
12	-31	-1	0.4338	78.016	$78.029 \pm 0.017$	0.548	0.142	$0.156 \pm 0.035$	$1362 \pm 387$	32.1
12	-31	0	0.4373	78.041	$78.045 \pm 0.018$	0.550	0.141	$0.160 \pm 0.036$	$1326 \pm 379$	16.4
12	-31	1	0.4416	78.066	$78.062 \pm 0.017$	0.553	0.140	$0.154 \pm 0.034$	$1354 \pm 382$	14.3
12	-30	-1	0.8397	79.185	$79.226 \pm 0.008$	0.757	0.040	$0.013 \pm 0.004$	$2127 \pm 377$	12.8
12	-30	1	0.8538	79.280	$79.310 \pm 0.009$	0.771	0.037	$0.027 \pm 0.006$	$977 \pm 236$	9.7

Same caption as Table A.1

**Table B.2.** Oscillation pattern of the RGB star KIC 2437976 in NGC 6791

$n_p$	$n$	$m$	$\zeta$	$\nu_{\text{as}}$ ( $\mu\text{Hz}$ )	$\nu$ ( $\mu\text{Hz}$ )	$x$	$\Gamma_{\text{as}}$ ( $\mu\text{Hz}$ )	$\Gamma$ ( $\mu\text{Hz}$ )	$H$ ( $\text{ppm}^2 \mu\text{Hz}^{-1}$ )	$R$
Radial modes										
8				75.045	$75.045 \pm 0.041$	0.013		$0.106 \pm 0.042$	$6520 \pm 3676$	7.8
9				83.284	$83.172 \pm 0.024$	0.001		$0.153 \pm 0.036$	$15645 \pm 4765$	31.3
10				91.382	$91.331 \pm 0.013$	-0.006		$0.100 \pm 0.017$	$22777 \pm 4443$	31.1
Dipole mixed modes										
8	-161	-1	0.8533	78.887	$78.893 \pm 0.008$	0.481	0.026	$0.022 \pm 0.006$	$10581 \pm 2376$	12.3
8	-160	-1	0.6438	79.234	$79.170 \pm 0.010$	0.514	0.064	$0.038 \pm 0.007$	$14647 \pm 2841$	11.9
8	-161	1	0.6511	79.343	$79.276 \pm 0.012$	0.527	0.063	$0.031 \pm 0.007$	$10930 \pm 2616$	9.6
8	-159	-1	0.7884	79.561	$79.519 \pm 0.008$	0.557	0.038	$0.026 \pm 0.006$	$14986 \pm 2978$	15.1
8	-160	1	0.8566	79.691	$79.671 \pm 0.009$	0.575	0.026	$0.023 \pm 0.006$	$6508 \pm 1802$	9.8
9	-146	-1	0.9726	86.115	$86.141 \pm 0.010$	0.362	0.005	$0.009 \pm 0.004$	$16564 \pm 5717$	7.6
9	-144	-1	0.7541	87.141	$87.185 \pm 0.010$	0.489	0.044	$0.054 \pm 0.013$	$20608 \pm 6137$	33.9
9	-145	1	0.7180	87.193	$87.191 \pm 0.009$	0.490	0.051	$0.049 \pm 0.011$	$23464 \pm 6034$	33.9
9	-143	-1	0.6110	87.503	$87.500 \pm 0.011$	0.528	0.070	$0.067 \pm 0.014$	$19703 \pm 4780$	29.1
9	-144	1	0.6404	87.550	$87.517 \pm 0.009$	0.530	0.065	$0.050 \pm 0.009$	$26627 \pm 5525$	29.1
9	-142	-1	0.8736	87.940	$87.943 \pm 0.007$	0.582	0.023	$0.009 \pm 0.004$	$21699 \pm 5272$	10.0
9	-143	1	0.8929	88.001	$87.989 \pm 0.006$	0.587	0.019	$0.009 \pm 0.004$	$29926 \pm 5102$	13.8
9	-141	-1	0.9588	88.486	$88.498 \pm 0.007$	0.649	0.007	$0.007 \pm 0.004$	$17180 \pm 3838$	8.1
9	-142	1	0.9622	88.537	$88.540 \pm 0.006$	0.654	0.007	$0.006 \pm 0.004$	$38360 \pm 5733$	18.3
10	-132	1	0.9463	94.663	$94.689 \pm 0.007$	0.402	0.010	$0.006 \pm 0.004$	$19058 \pm 3790$	9.7
10	-131	-1	0.9440	94.692	$94.708 \pm 0.008$	0.405	0.010	$0.005 \pm 0.004$	$15841 \pm 4952$	7.6
10	-131	1	0.7969	95.259	$95.216 \pm 0.009$	0.466	0.037	$0.034 \pm 0.008$	$21679 \pm 5266$	18.4
10	-130	-1	0.7827	95.284	$95.257 \pm 0.009$	0.471	0.039	$0.033 \pm 0.008$	$19865 \pm 4877$	20.4
10	-130	1	0.5518	95.692	$95.630 \pm 0.008$	0.517	0.081	$0.025 \pm 0.005$	$42908 \pm 7274$	26.4
10	-129	-1	0.5572	95.709	$95.633 \pm 0.008$	0.517	0.080	$0.027 \pm 0.006$	$39045 \pm 6386$	26.4
10	-129	1	0.8453	96.161	$96.162 \pm 0.007$	0.582	0.028	$0.009 \pm 0.004$	$29045 \pm 5946$	21.6
10	-125	0	0.9891	98.575	$98.551 \pm 0.008$	-0.128	0.002	$0.004 \pm 0.004$	$15436 \pm 11044$	7.5
11	-118	-1	0.8082	103.469	$103.439 \pm 0.010$	0.467	0.034	$0.023 \pm 0.006$	$6844 \pm 1785$	9.8
12	-108	1	0.7958	111.880	$111.821 \pm 0.012$	0.487	0.037	$0.022 \pm 0.006$	$5310 \pm 1445$	7.9
12	-105	-1	0.9174	113.342	$113.329 \pm 0.007$	0.670	0.015	$0.006 \pm 0.004$	$16746 \pm 4518$	8.6

Same caption as Table A.1